(2)

FhG

Fraunhofer-Gesellschaft

Fraunhofer-Institut für
Werkstoffmechanik

(2)

FRAUNHOFER-INSTITUT FÜR WERKSTOFFMECHANIK
Wöhlerstraße 11, 7800 Freiburg

V 10/88

FRACTURE BEHAVIOUR UNDER IMPACT II

S. Winkler

Contract Number DAJA45-85-C-0047

Final Report

October 1985 - October 1987

Prepared for

European Research Office
of the U.S. Army
London

IWM-Projekt Nr.303 054

67 pages
4 tables
46 figures

The Research reported in this document has been made possible through the support and sponsorship of the U.S. Government through its European Research Office of the U.S. Army. ~~This report is intended only for the internal management use of the Contractor and the U.S. Government~~.

Unclassified
SECURITY CLASSIFICATION OF THIS PAGE

REPORT DOCUMENTATION PAGE

Form Approved
OMB No 0704-0188
Exp Date Jun 30 1986

1a REPORT SECURITY CLASSIFICATION Unclassified	1b RESTRICTIVE MARKINGS
2a SECURITY CLASSIFICATION AUTHORITY	3 DISTRIBUTION/AVAILABILITY OF REPORT Approved for public release; distribution unlimited
2b DECLASSIFICATION/DOWNGRADING SCHEDULE	
4 PERFORMING ORGANIZATION REPORT NUMBER(S)	5 MONITORING ORGANIZATION REPORT NUMBER(S) R&D 3012A-AN
6a NAME OF PERFORMING ORGANIZATION Fraunhofer-Institut für Werkstoffmechanik 6b OFFICE SYMBOL (If applicable)	7a NAME OF MONITORING ORGANIZATION USARDSG(UK)
6c ADDRESS (City, State, and ZIP Code) Wöhlerstrasse 11 D-7800 Freiburg Germany	7b ADDRESS (City, State, and ZIP Code) Box 65 FPO New York 09510-1500
8a NAME OF FUNDING/SPONSORING ORGANIZATION USARDSG(UK) ERO 8b OFFICE SYMBOL (If applicable) AMXSN-UK-RA	9 PROCUREMENT INSTRUMENT IDENTIFICATION NUMBER DAJA45-85-C-0047
8c ADDRESS (City, State, and ZIP Code) Box 65 FPO New York 09510-1500	10 SOURCE OF FUNDING NUMBERS PROGRAM ELEMENT NO: 61103A PROJECT NO: 1L161103BH57 TASK NO: 06 WORK UNIT ACCESSION NO:
11 TITLE (Include Security Classification) (U) Fracture Behavior Under Impact II	
12 PERSONAL AUTHOR(S) S. Winkler	
13a TYPE OF REPORT Final 13b TIME COVERED FROM Oct 85 TO Oct 87	14 DATE OF REPORT (Year, Month, Day) 1987, October 15 PAGE COUNT 67
16 SUPPLEMENTARY NOTATION	

17 COSATI CODES			18 SUBJECT TERMS (Continue on reverse if necessary and identify by block number)
FIELD	GROUP	SUB-GROUP	(see reverse)
19	04		
20	11		

19 ABSTRACT (Continue on reverse if necessary and identify by block number)

(see reverse)

20 DISTRIBUTION/AVAILABILITY OF ABSTRACT ☒ UNCLASSIFIED/UNLIMITED ☒ SAME AS RPT ☐ DTIC USERS	21 ABSTRACT SECURITY CLASSIFICATION Unclassified
22a NAME OF RESPONSIBLE INDIVIDUAL Dr. Fritz H. Oertel, Jr.	22b TELEPHONE (Include Area Code) 01-409 4423 22c OFFICE SYMBOL AMXSN-UK-RA

DD FORM 1473, 84 MAR

83 APR edition may be used until exhausted
All other editions are obsolete

SECURITY CLASSIFICATION OF THIS PAGE
Unclassified

18. SUBJECT TERMS

Impact loading, Dynamic tensile stress intensity factor, Dynamic shear stress intensity factor, Crack instability, Dynamic tensile fracture, Dynamic shear fracture, Impact tensile fracture toughness, Impact shear fracture toughness, Adiabatic shear bands, Shear wave loading, Shadow optical method of caustics

19. ABSTRACT

The behaviour of cracks loaded by impact generated stress pulses is investigated. Depending on the impact arrangement tension or shear loading at extremely high rates of the stress intensity factor can be realized.

With specimens of a high strength steel a steep increase of the tensile fracture toughness has been observed with times-to-fracture decreasing to about 5us. This has been measured with an improved shadow optical technique in reflection. The assumption of an incubation time is used to explain this behaviour.

A novel impact geometry is introduced for loading cracks under shear by pressure waves in combination with inertial forces. Interesting shear phenomena were found: adiabatic shear bands or dynamic shear cracks are generated at the crack tip . For their production temperatures in the melting range must be generated by a very high lateral strain gradient and remain concentrated to a small volume which moves with the compression field. To maintain this either a low heat conduction or a very rapid increase of the compression field is required. This explains that a threshold in the compression (i.e. in impact velocity) must be exceeded.

Tensile loading of a crack up to $4*10^5$ MPa$\sqrt{m}$/s has been achieved by a superposition of shear waves generated at the specimen boundaries by a passing compression pulse. This particular succession of compression and tension is the reason for a fast rising tensile loading at one of the two crack tips.

1. INTRODUCTION

In a previous research project "Fracture Behaviour Under Impact (I)" the physical behaviour of cracks under impact loading has been investigated: Specimens with single edge cracks or arrays of multiple cracks were loaded by time dependent tensile stress pulses moving perpendicular to the crack direction. The pulses were produced by impinging projectiles. Two kinds of experiments were performed: Firstly, the projectile hits a base plate which in turn loads a specimen with crack in tension. Secondly, the specimen is directly impacted by the projectile. After the passage of a compressive stress pulse through specimen and impactor stresses are built up by reflected relief waves which load the crack in tension. Specimens made from a transparent model material and a high strength steel were investigated. The shadow optical method of caustics in combination with high speed photography was used to measure the dynamic stress intensity factor K_I at the tip of the crack as function of time. The stress intensity factor at onset of rapid crack propagation, i.e. the dynamic fracture toughness K_{Id}, was determined and discussed in relation with the loading history and the time to fracture.

The technical background, the experimental set-up, the measuring procedures, and the results of these investigations have been described in detail in the final report of the first contract [1]. The main findings of this previous research work are summarized here, since they represent the basis for this follow-on research, "Fracture Behaviour Under Impact II".

(1) When testing single-edge cracked specimens made from the model material Araldite B under both, base plate and direct impact loading conditions times-to-fracture down to 6 µs have been achieved. Up to this loading rate the observed impact fracture toughness K_{Id} did not show a dependence on loading rate. These results, however, are in contradiction to data obtained by Ravi-Chandar and Knauss [2] who reported a very strong increase of the impact fracture toughness K_{Id} for another model material, Homalite 100, for times-to-fracture below 30 µs.

(2) Experiments with specimens made from a high strength Ni-maraging steel (German designation X2 NiCoMo 18 9 5), however, resulted in a strong dependence of K_{Id} from loading rate for short times-to-fracture. With regard to the static fracture toughness K_{Ic} these data first show an unexpected reduction in toughness for times-to-fracture in the range of 15 µs to 10 µs, but an unexpected very rapid increase if the time-to-fracture is decreased further down to 6 µs. The

dynamic toughness then becomes even larger than the static one. The observed experimental findings have been explained on the basis of a novel instability criterion which is based on the assumption of an incubation time for a crack to start propagating. This incubation time is believed to be a material dependent property.

(3) To study the dynamic interaction of multiple crack configurations under impact loading conditions, two parallel cracks of distance h in Araldite B specimens were loaded by a tensile stress pulse generated in the base plate test arrangement. Shadow optics and short time cinematography revealed a rather complex time dependent stress intensity factor history. For early times much larger asymmetric mode II (in-plane shear) contributions are prevailing in the local crack tip fields than under equivalent static conditions, and a periodic exchange of the crack tip strain energy from one crack to the other takes place. Only for long times after impact the overall situation becomes similar to the one under static loading conditions.

(4) Tests on impact loaded specimens with cracks of different lengths did not show an influence of crack length on stress intensity history when early times after impact were considered. Only at later times for the same loading pulse the larger cracks exhibited larger stress intensity factors than the shorter ones as one would expect from static considerations. Obviously, in the regime of small ratios of "time" to "crack length", besides the load amplitude it is the parameter "time" and not the "crack length" which controls the fracture behaviour.

Within the follow-on project "Fracture Behaviour Under Impact II" the described research work should be continued in order to supplement the earlier results and to add research on the newly detected phenomenon of dynamic shear fracture under high rate loading. In detail, the following research tasks were defined:

TASK 1: Performance of additional impact loading experiments on the high strength steel and postevaluation of all results to substantiate the observed increase in fracture toughness with decreasing loading time for this material. Impact testing of the material Homalite 100 in order to analyze the discrepancy of the Araldite B results with the results of Ravi-Chandar and Knauss [2].

TASK 2: Investigation of the mechanical and material conditions in impact shear tests and determination of the shear stress intensity factor K_{II} in Araldite B and the high strength steel specimen.

TASK 3: Investigation of the phenomenon of "crack propagation in an impacted specimen during the compression phase". This method may advance to a technique for reduced time-to-fracture experiments.

TASK 4: Improvement of the accuracy of the shadow optical technique applied in reflection at high rate impact conditions.

TASK 5: Additional experiments to verify the independence of the stress intensity factor from crack length for early times after impact.

During the execution of the research program "Fracture Behaviour Under Impact (II)" the following changes were made:

Since it was not possible to make available in time test pieces of the same batch of Homalite 100 or test pieces of Ravi-Chandar and Knauss [2] (which are still under evaluation at CALTECH) the investigations on this material had to be abandoned.

Due to currency exchange rate problems minor parts of the program had to be shortened, especially in order not to reduce more interesting parts too much, work on Task 5 was not carried out.

2. WORK ON RESEARCH TASK 1: DEPENDENCE OF IMPACT FRACTURE TOUGHNESS ON LOADING RATE

With the improved shadow optical arrangement (see Task 4) experiments on 18 Ni maraging high strength steel specimens have been performed under direct impact loading to measure the impact fracture toughness K_{Id} at increased impact velocities. These experiments were aimed to generate additional data points in order to verify the steep increase in the fracture toughness observed for loading rates which exceed a certain limit (see [1], sect. 5.2).

Five experiments (# 862 to # 866) have been performed in the IWM gas gun loading device with impact velocities up to 24 m/s. Fig. 1 shows the experimental arrangement. For all impact velocities the shadow optical pictures were of sufficient quality to allow the determination of the critical stress intensity factor at onset of rapid crack propagation. The test conditions and the results of the experiments performed are summarized in Table 1. This table contains also the previous data in a revised form which follow from a reevaluation of the shadow optical pictures based on results described in chapter 3 of this report.

All data (# 852 to # 866) are collected in Fig. 2. The new experiments (full squares) also show times-to-fracture down to less than 5 µs. The revised previous data are marked by full circles.

For comparison, data obtained at lower loading rates and at quasistatic loading conditions are also shown in Fig.2 (open symbols). These data were measured with drop weight and precracked Charpy tests. The shadow optical method was used in most of these experiments for determining the impact fracture toughness. With Charpy specimens, however, the concept of impact response curves [5] was applied.

The new results agree with the earlier data points. Thus, the speculations and conclusions presented in the final report of the previous project [1] are substantiated by the new data: The previously observed increase in the fracture toughness with increasing loading rate (decreasing time-to-fracture) for the investigated material is confirmed. This finding is also in agreement with the results of Ravi-Chandar and Knauss [2] for the material Homalite 100. They found an increase of the fracture toughness beginning at a time-to-fracture of ~30 µs. They were able to measure down to ~15 µs where the static fracture toughness was doubled. This indicates that this effect is material dependent. It can, therefore, be expected that materials exist with a very small loading rate sensitivity. This was the case with the material Araldite B [1]. In the investigated time regi-

me down to about 7 µs a deviation from the static fracture toughness could not be found.

An explanation for this phenomenon was given earlier ([1], Section 5.2) by the conception of an incubation time, which is the time the crack needs to experience a supercritical stress intensity factor, $K > K_{crit}$, before it starts to propagate rapidly (see the schematic representation in Fig. 3). The influence of this incubation time is negligible for low strain rates. It becomes, however, important with times-to-fracture being of the same order of magnitude with the incubation time. During this time delay an overshoot in stress intensity appears which leads to the measured effect. If an increase in the fracture toughness by a factor of 2 is observed it can roughly be assumed that the incubation time is half the measured time-to-fracture (Fig. 3). With the data of Fig. 2 an incubation time in the range of 1 to 2 µs is estimated, whereas from the data of Ravi-Chandar and Knauss [2] an incubation time of about 8 µs is deduced for the material Homalite 100.

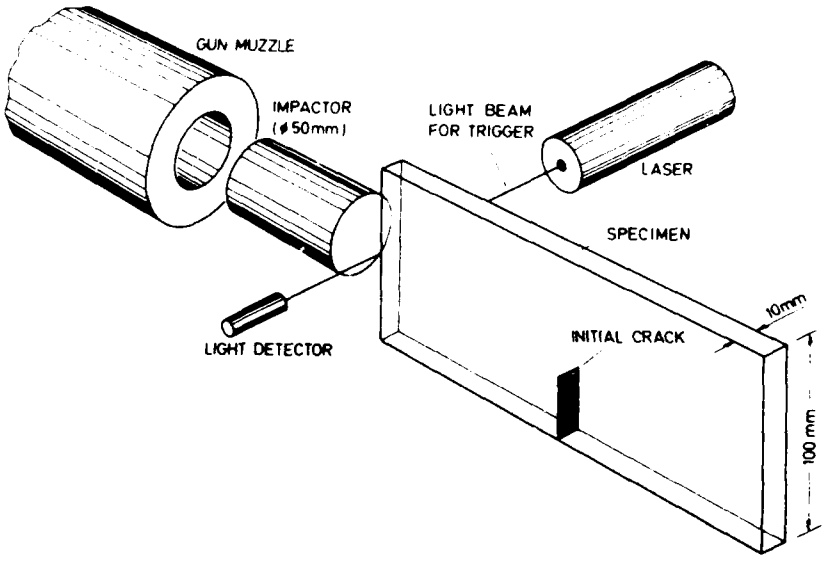

Fig. 1 Dynamic tensile loading arrangement (direct impact loading)

Shot #	Shot v_o m/s	Specimen B mm	Specimen a mm	Results t_f µs	Results K_{Id} MPa$\sqrt{m}$
852	19.6	17.0	51.0	5.0	64
853	19.7	18.2	50.0	5.5	62
854	19.5	16.8	50.5	6.5	52
855	19.8	17.3	49.7	5.5	60
856	9.6	16.8	50.3	10.0	47
857	27.8	18.4	50.3	4.5	69
861	47.0	18.5	49.8	4.0	84
862	74.0	18.5	49.6	4.7	89
863	20.6	18.5	50.7	5.3	58
864	10.9	18.4	50.0	8.5	40
865	48.4	17.9	50.3	5.0	81
866	38.6	17.9	50.5	5.0	73

List of symbols:

v_o = impact velocity
B = specimen thickness
a = length of initial fatigue crack
t_f = time-to-fracture
K_{Id} = impact fracture toughness

Dimensions of the specimen:
length L = 250mm, width W = 100mm

Dimensions of the projectile:
length L = 125mm, mass m = 1.90kg

Table 1 Test conditions and results of fast tensile experiments (mode I) with the high strength 18 Ni maraging steel

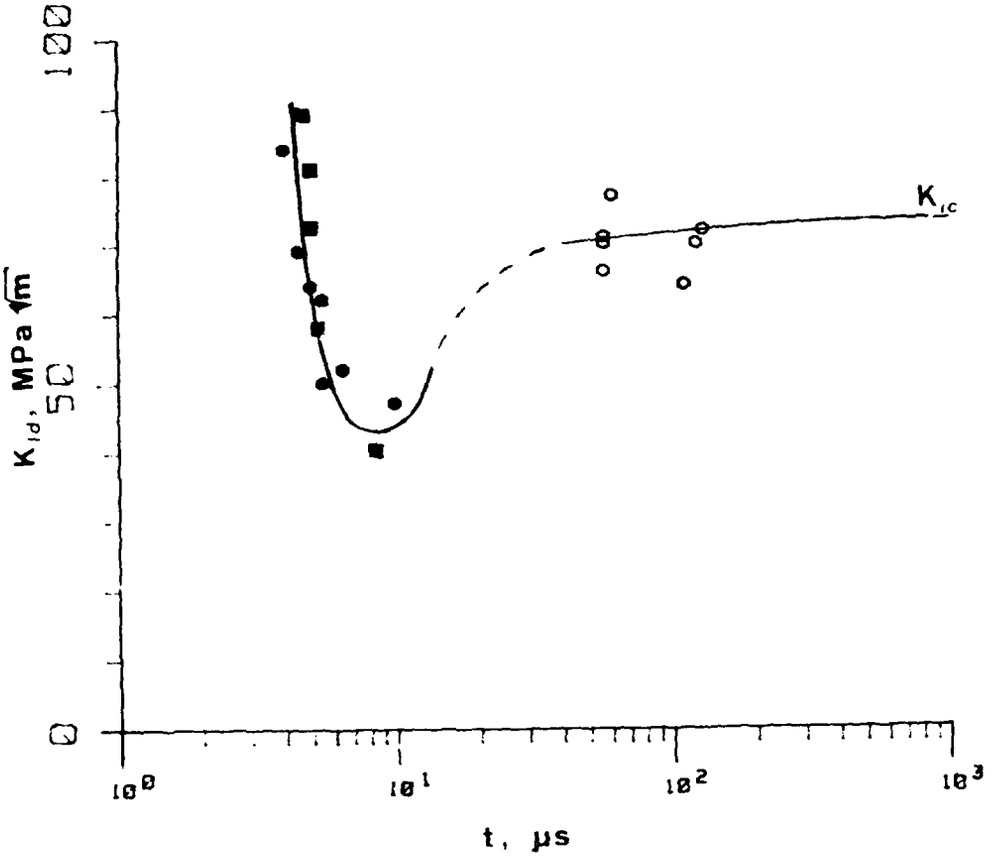

Fig. 2 Impact fracture toughness data of the high strength steel X2 NiCoMo 18 9 5 for different loading rates

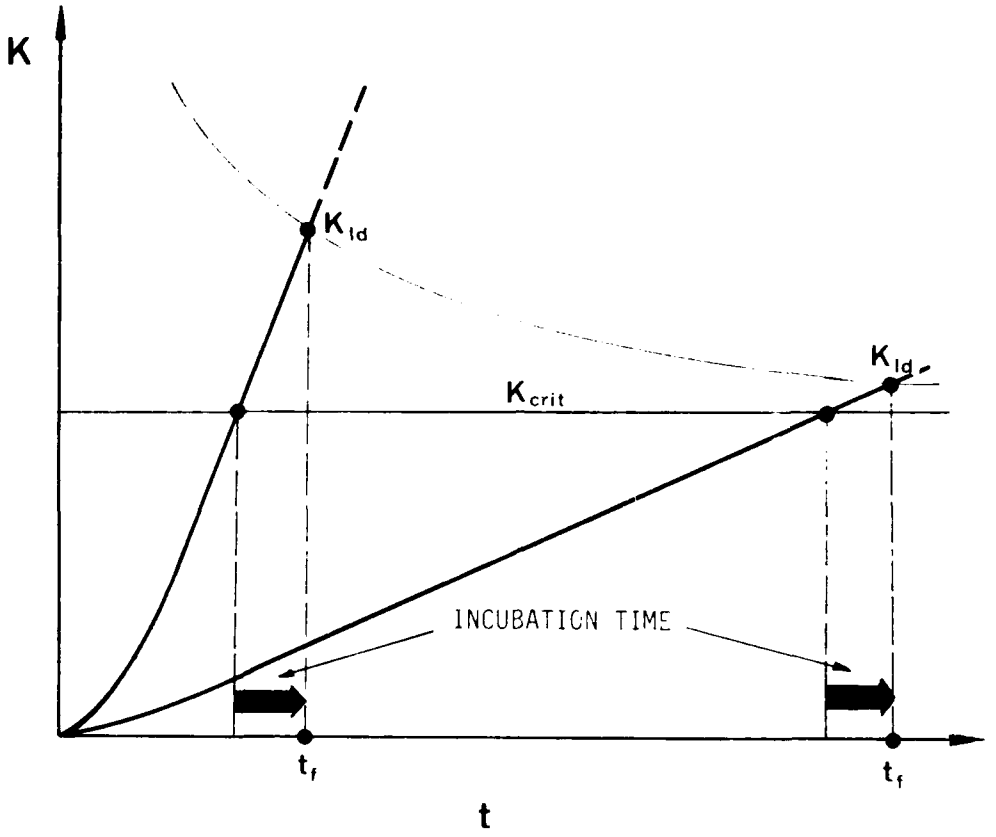

Fig. 3 Influence of the incubation time on the instability behaviour of cracks for different rates of loading

3. WORK ON RESEARCH TASK 2: INVESTIGATION OF DYNAMIC SHEAR FRACTURE

A dynamic shear loading method has been developed. Inertia is used instead of sophisticated loading devices as required in static experiments. The idea is that a crack dynamically loaded on one side parallel to its surface experiences a pure mode II loading as long as the material on the other side of the crack "does not know" about this impact event.

3.1 Shear Loading Technique

Specimens were used with two parallel edge-cracks (or edge-notches) being apart by a distance h. The specimen is impacted at its notched edge by a projectile with diameter d equal to the distance h of the two cracks (see Figs. 4 and 6). It was expected that the longitudinal compressive wave in the middle part of the specimen would generate mode II loading conditions at the crack tips. The specimen is free movable after impact. A holding fixture was designed to fix the position for a precise impact but to release the specimen shortly after impact.

Later on also a modified type of specimens (Fig. 5) was introduced containing one notch only. These asymmetric specimens are much easier to fabricate and require less material.

With the incident compressive wave produced by the impinging projectile lateral displacements are associated. These may cause disturbances: Cracks with surfaces being in contact to each other or being not too far apart of each other can be closed and even compressed by these lateral displacements, thus leading to uncontrollable friction effects between the crack surfaces. As a consequence, the formation of a shear concentration at the crack tip can be disturbed. The possible influences due to these lateral displacements have been investigated by using notches with a finite opening of the notch surfaces. Then the primary compression wave can generate a compressive mode I stress concentration at the notch tip which can be visualized and quantitatively evaluated by the shadow optical method of caustics.

Cylindrical steel projectiles of 50mm diameter were used to impact the specimens. The projectiles are accelerated by the IWM gas gun to velocities ranging from 10m/s to about 100m/s. For specimens with cracks being less than 50mm apart, projectiles were used which at their front end had a correspondingly reduced diameter (see Fig. 11). Sometimes also modified specimens were used (see Fig. 12). Typical

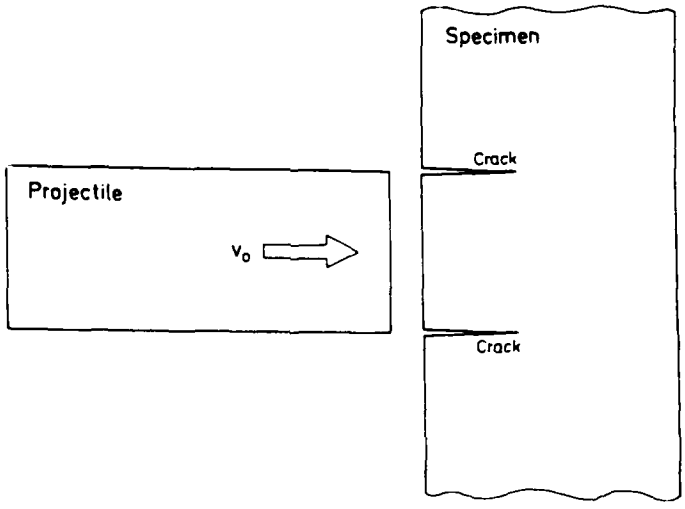

Fig. 4 Dynamic shear loading arrangement (schematically): symmetric specimen

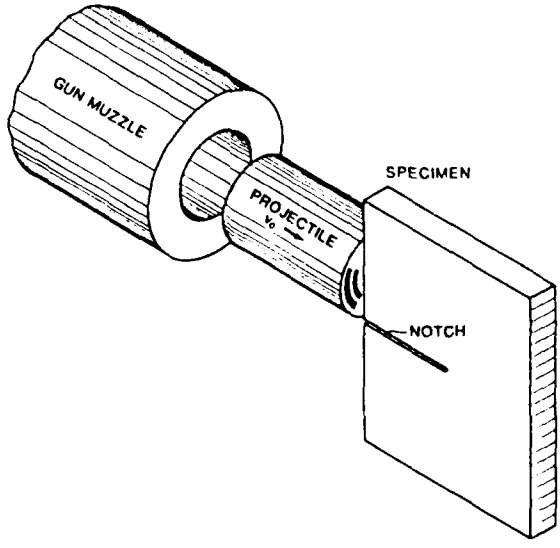

Fig. 5 Dynamic shear loading arrangement: asymmetric specimen

measurements of the specimens were 100mm * 200mm and 150mm * 300mm. The specimen thicknesses were usually 10mm. The crack lengths were in the range of 50mm to 75mm.

3.2 Experimental Results

Experiments were performed with specimens made from different materials. Mainly the two transparent model materials Polymethylmethacrylat (PMMA) and the epoxy resin Araldite B were used. In these cases the shadow optical method of caustics could be applied in transmission. For the high strength steel 42 NiCrMo 13 4, however, the shadow optical method can only be applied in reflection requiring one of the surfaces being prepared specially by grinding, lapping, and polishing to achieve a mirrored front surface.

3.2.1 Loading Phase

To get a first survey on the crack (or notch) tip loading conditions, experiments have been performed with specimens made from PMMA. PMMA generates single caustics which can be evaluated in an easier way than double caustics observed with the birefringent material Araldite B. Steel specimens also generate single caustics, but have only been used for the main experiments due to the extensive costs for specimen preparation. Double and single notched specimens have been used.

In order to measure mode I stress concentrations as well as shear mode II stress intensifications, shadow optical patterns have been observed with a transmission arrangement in a virtual image plane (see Appendix). Then compressive mode I stress concentrations result in a dark shadow spot which can be evaluated in an easier way than the light concentration patterns which would result in the real image plane. The mode II shadow patterns, however, remain the same except for a mirror-like transversion. The shadow optical recording arrangement is schematically shown in Fig. 6.

Typical series of shadow optical photographs from PMMA experiments are shown in Fig. 7 for a double-notch specimen (h = 30mm) and in Fig. 8 for a single-notch specimen. A comparison of the shadow patterns shows the same behaviour for both specimens. With increasing time an almost pure mode II loading builds up. Only for the early time range disturbances due to lateral compressions are observed. At very early times, the resulting compressive mode I loading at the crack tip is indeed dominant. With increasing time and rising mode II loads, however, the disturbing compressive mode I contributions become negligible. The last pic-

tures of the "upper" notch in Fig. 7 indicate the beginning of the instability process: The mode II caustic changes slightly exhibiting the characteristic light concentration pattern (see Appendix) as is typical for a tensile mode I stress concentration under this observation condition. In Fig. 7 the lower notch still is stationary.

Since the observed behaviour at the tip of the crack of the dynamicly loaded symmetric double-notch specimen is obviously the same as for the asymmetric single-notched specimen, in most of the experiments asymmetric single notch specimens were used. They are much easier to machine, in particular when steel specimens had to be used.

The loading rate dK/dt was measured in experiments with specimens made from Araldite B and from the high strength steel X2 NiCoMo 18 9 5. With the transparent Araldite B specimens the shadow optical transmission arrangement for recording virtual shadow patterns has been used (i.e. the same recording arrangement as used with PMMA specimens). With steel specimens, however, the reflection arrangement with recording real shadow patterns was applied (Fig. 6).

Quantitative data on the dependence of the stress intensity factor K_{II} as a function of time t are shown in Fig. 9 of specimens with blunted notch tips. The impact velocities have been 12m/s for Araldite B and 13m/s for steel. Since steel specimens permit higher impact velocities before damage occurs at the contact area between the projectile and the specimen, data are also reported for the increased impact velocity 33m/s. The highest observed average stress intensification rates dK_{II}/dt are about $2*10^5$ MPa$\sqrt{m}$/s for Araldite B and $2*10^7$ MPa$\sqrt{m}$/s for steel. A rough estimate of the times-to-fracture resulting from these loading rates assuming fracture to initiate at a toughness level corresponding to the static mode I fracture toughness K_{Ic} ($\approx$ 0.6 MPa$\sqrt{m}$ for Araldite B and $\approx$ 70 MPa$\sqrt{m}$ for the steel X2 NiCoMo 18 9 5) yields values of $\approx$ 5 µs in both cases.

In drop-weight tests with three-point-bend specimens of similar size times-to-fracture of the order of 100µs are observed. Thus, the loading rates dK_{II}/dt obtained with the present shear loading arrangement as well as with the tensile loading mode described in chapter 2 are more than one order of magnitude faster than those obtained by drop weight tests. This is a consequence of the direct crack tip loading by the fast expanding stress field produced by the impactor. In the three-point-bend test, however, the crack tip in the specimen is loaded by bending where the bending is built up by the transversal oscillation of the entire specimen. The frequency of this oscillation and also the

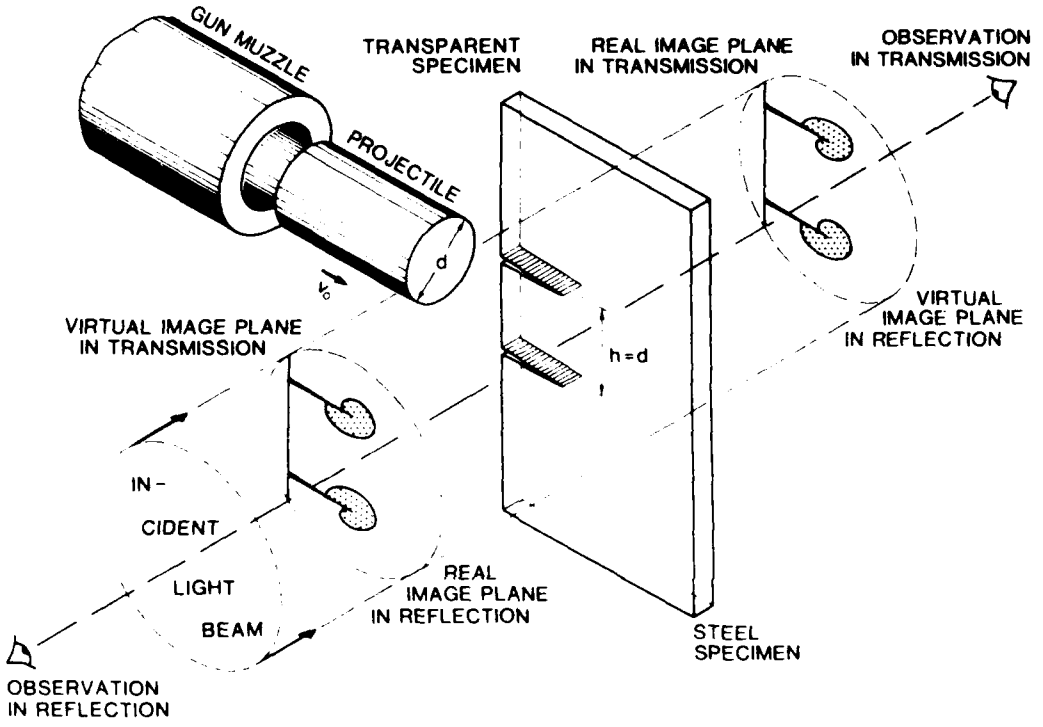

Fig. 6 Experimental set-up: dynamic shear (mode II) loading arrangement and different arrangements for shadow optical observation

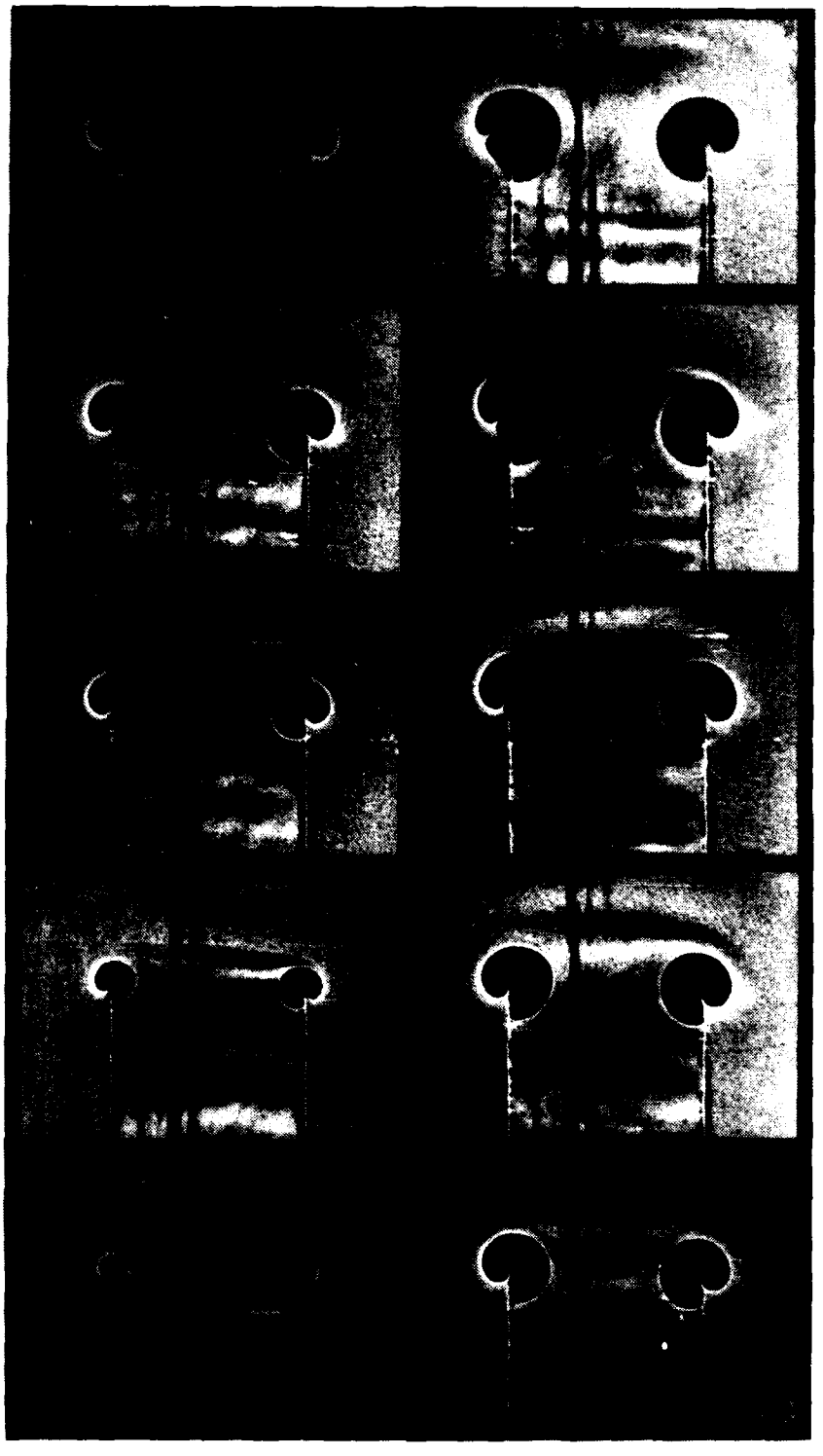

Fig. 7 High speed series of shadow photographs: double-notch specimen under shear loading (PMMA, virtual image plane, picture interval time 2 μs)

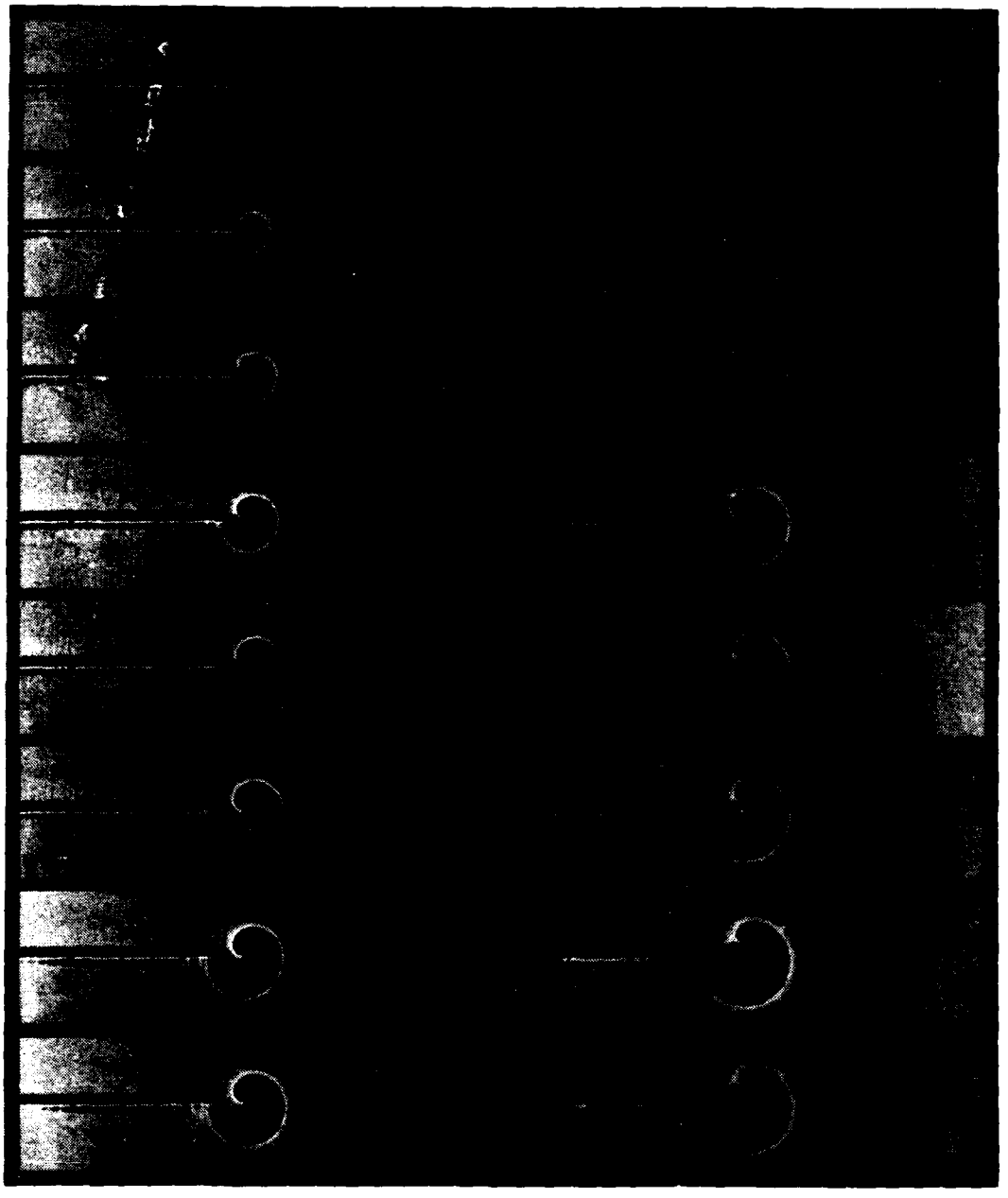

Fig. 8 High speed series of shadow photographs; single-notch specimen under shear loading (PMMA, virtual image plane, picture interval time 2 us)

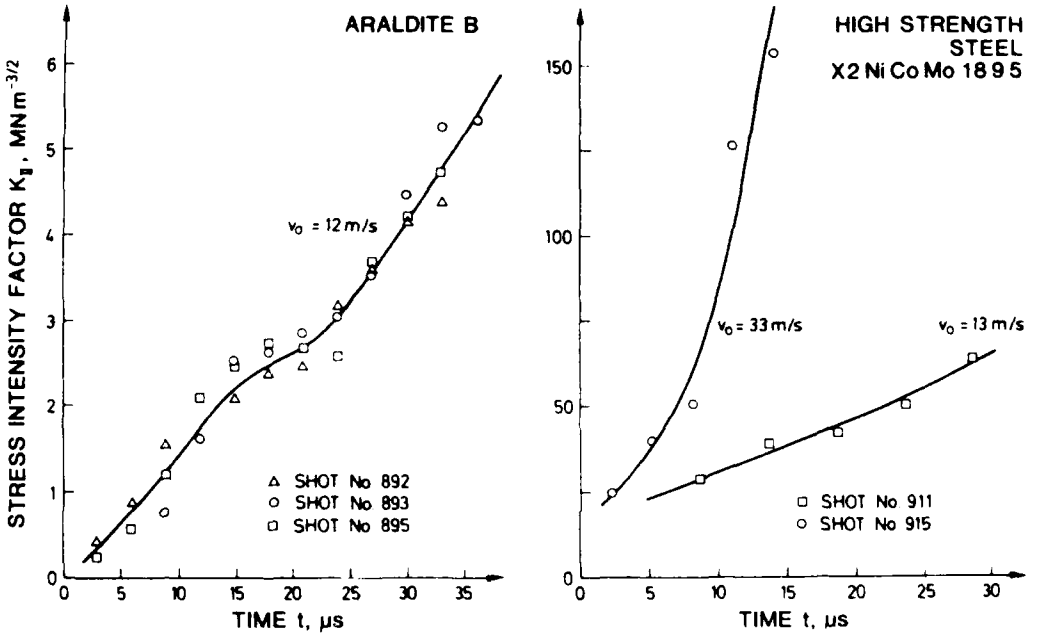

Fig. 9 Dynamic shear stress intensity factor K_{II}

increase in crack loading depends on specimen size and is relatively slow compared to wave propagation times.

5.2.2 Crack Propagation Phase

The crack propagation obtained under the described loading conditions has been investigated with specimens made from PMMA, Araldite B and the high strength steel. Under static test conditions a crack will propagate in a direction perpendicular to the maximum tensile stress at the crack tip. For static pure mode II loading the crack starts to extend into a direction which includes an angle of about 70° with the orientation of the initial crack and continues propagating in the tensile mode I fracture mode. This is in agreement with theoretical results. The same behaviour was also observed in the dynamic experiments.

In order to visualize the expected tensile (mode I) loading at the crack tip shadow patterns now have been recorded in the opposite image planes than reported in section 3.2.1. The camera was focussed on a real image plane for the shadow optical transmission arrangement with PMMA and Araldite B specimens, and on a virtual image plane for the reflection arrangement with steel specimens (see also Fig. 5 and Appendix). Typical results for the considered materials are presented in Figs. 10, 11, and 12. The caustics in Figs. 10 and 11 indicate that the cracks indeed propagate under an almost undisturbed tensile mode I loading. And similar to the static behaviour the crack propagation is inclined with regard to the direction of the original initial crack. Some typical results for crack paths are shown in Fig. 12. In the experiments with PMMA and Araldite B specimens the observed angle is in most cases very close to the expected value of 70°. The angle found with the steel specimen is somewhat smaller, but within the scatter band normally found with corresponding static experiments. The observed crack propagation directions are an additional indication that the initial notches had been loaded by an almost undisturbed pure mode II loading.

In addition to the crack tip shadow patterns the photographs obtained with the steel specimen in reflection (Fig. 11) show patterns of mechanical waves which emanate from the tip of the propagating crack. The propagation velocity indicates that these are Rayleigh waves preceded by almost not visible longitudinal waves. The deformations of the specimen surface caused by the waves become visible by the shadow optical technique. The photographs of Fig. 10, however, taken in transmission do not exhibit waves in the same

distinct way. Only when the crack starts propagating, in the very first pictures, waves are observable. The conclusion is that the shadow optical method in reflection is much more sensitive to surface distortions than in transmission.

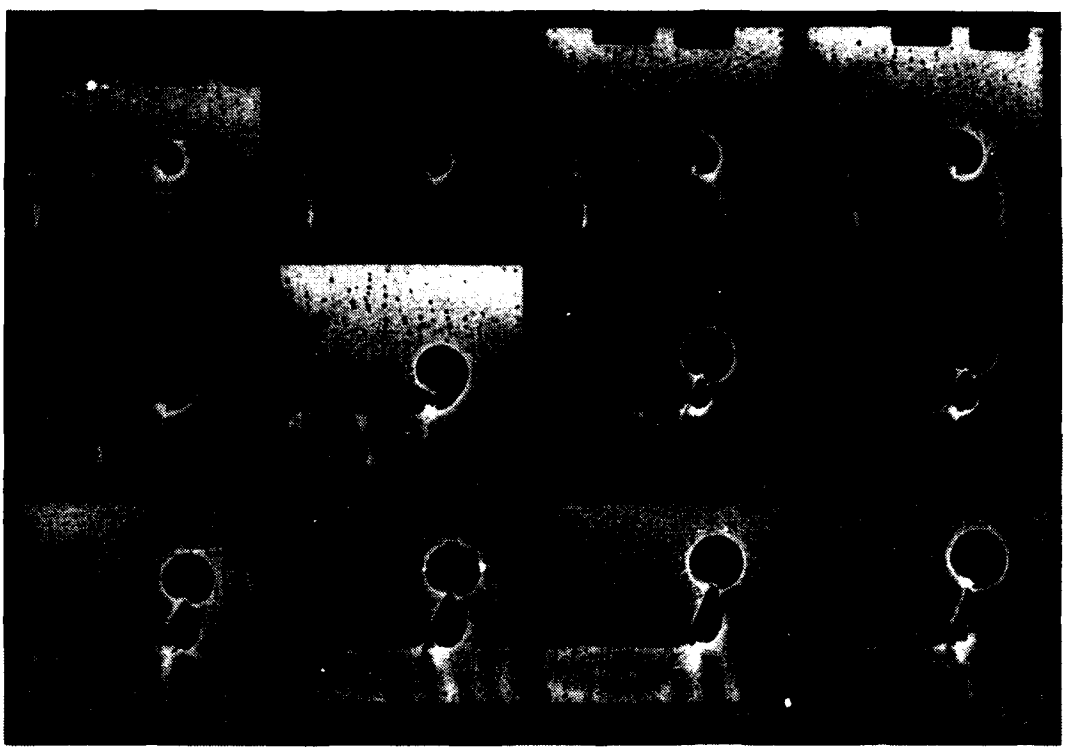

Fig. 10 Crack propagation initiated from a shear loaded notch (Araldite B), shadow optical technique in transmission

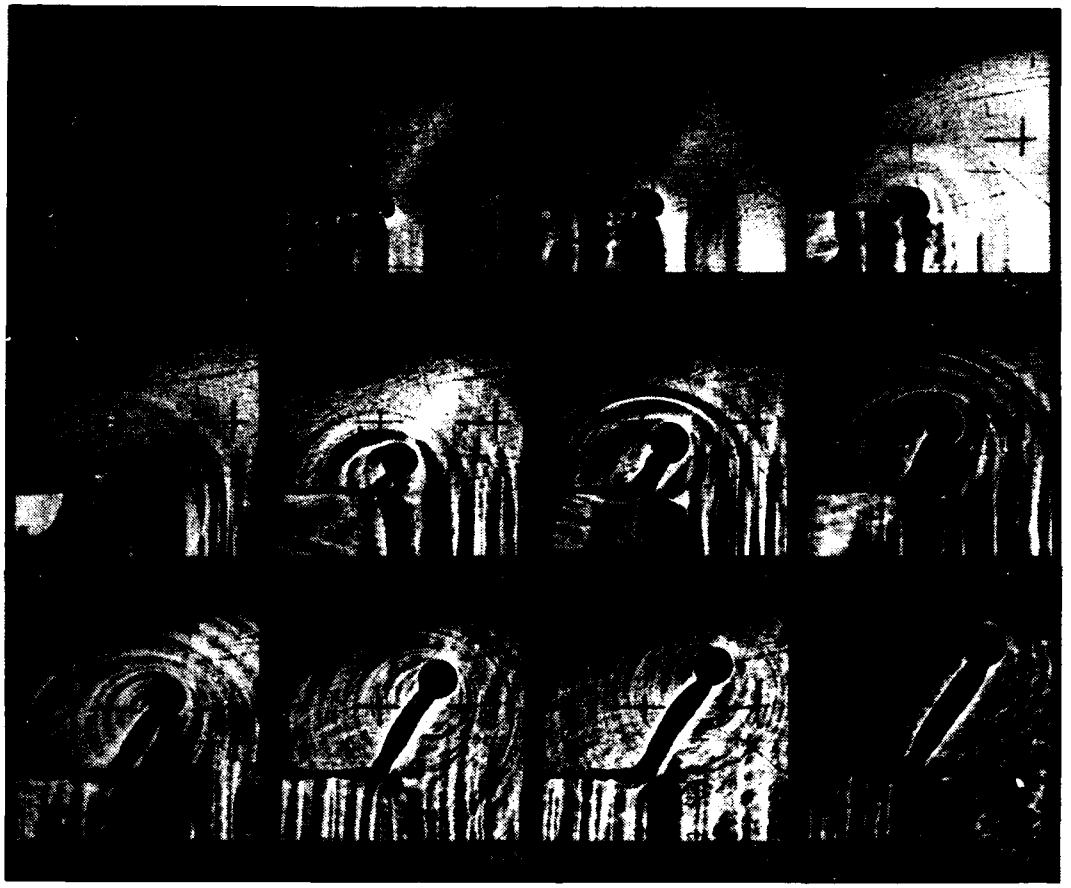

Fig. 11 Shadow optical pictures (reflection technique) of a crack propagation initiated from a shear loaded notch (steel X2 NiCoMo 18 9 5)

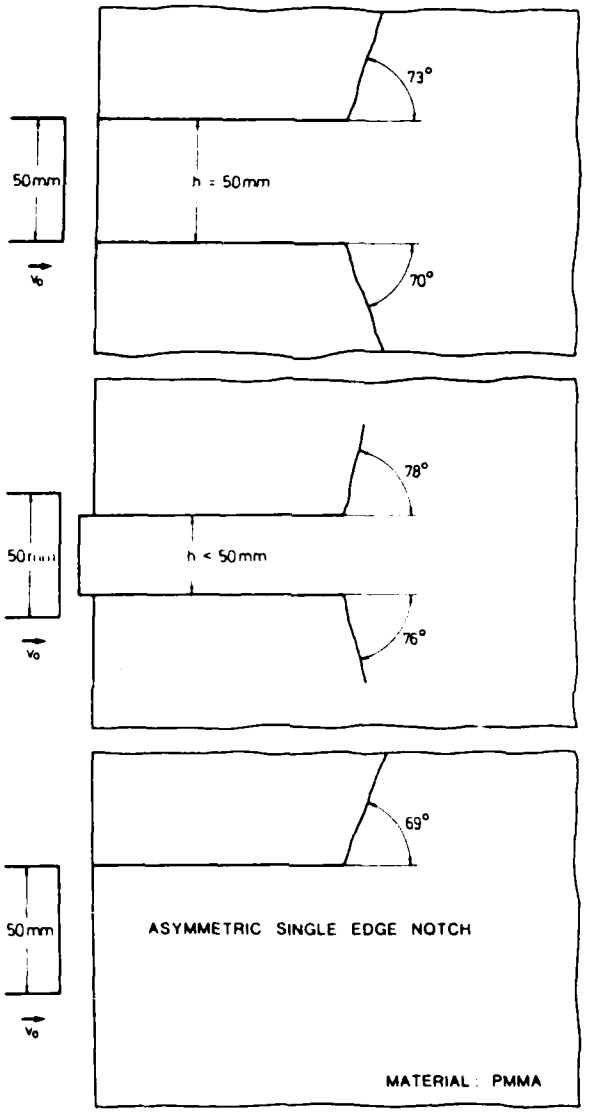

Fig. 12 Crack propagation paths in PMMA-specimens, shots # 880, # 883, # 904

3.2.3 Dynamic Shear Crack Propagation

A surprising effect was found with the crack propagation behaviour of high strength steel specimens impacted above a certain threshold velocity: material separation occurred under shear mode loading with new phenomena in the fracture surface. The investigation of this new effect was a major part of the total research program and is described in this section.

In the series of experiments which has been performed to understand this new effect two parameters were varied, the impact velocity and the notch tip bluntness. Both parameters were expected having an influence on the crack tip strain concentrations.

Experimental results are given in Fig. 13. The crack paths (length and direction) are compiled in a notch tip radius versus impact velocity diagram. Some of the cracks with low crack tip acuity (0.05 mm and 0.15 mm) and impacted at lower velocities (30 to 40 m/s) show the same behaviour as in the "slow" experiments of section 3.2.2. These cracks propagated in a direction 70° from the ligament and away from the stress field produced by the impactor. All the other notches or cracks developed the new type of "dynamic shear fractures" which propagated almost straight along the ligament. The deviation from the straight path is between 8° and 18° but opposite to the others into the impactor compression field.

In the experiments with the maraging steel described in this section the specimens usually broke in two or three parts mainly by fractures which were identified to be tensile fractures. These, however, were in most cases preceded by the new type of dynamic shear fracture (for exceptions see Table 2, fracture mode). An example is shown in Fig. 14. A photograph of the middlepart of the specimen containing the notch and the crack path is Fig. 14a. The crack started almost straight from the notch and propagated as a shear crack over a distance of 17mm. A photograph of this surface is Fig. 14b. After this the crack did not only change its direction but also the fracture mode. It propagated as a tensile fracture, breaking the specimen in two parts, and generating thereby a typical tensile fracture surface (Fig. 14c). The direction of this following tensile fracture varies in different experiments. It is assumed that this fracturing occurs in a late phase e.g. by bending during the catching process.

The test data and the experimental findings of this program are listed in Table 2. The length a_s of the dynamic shear crack was measured. a_s varies from experiment to experiment

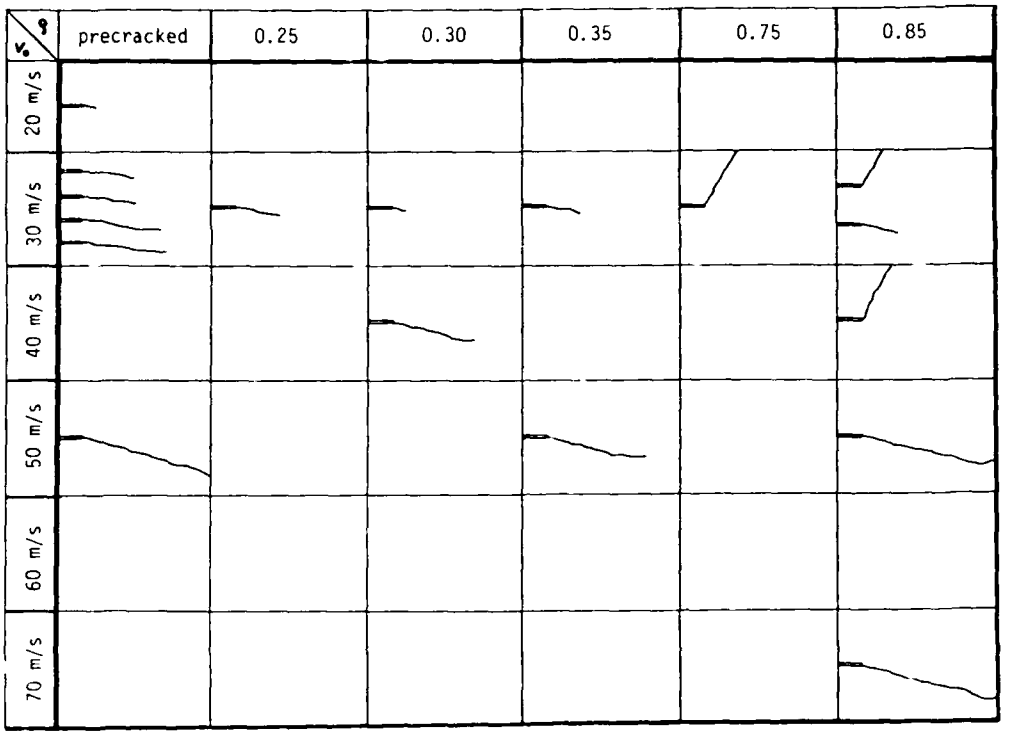

Fig. 13 Compilation of crack paths in shear experiments on high strength steel specimens

but obviously increases with increasing impact velocity. The last column of Table 2 tells details of the resulting fractures. For shot numbers 908 to 912 only one specimen was used since no fracture occurred until shot # 912. In two cases the initial shear crack was followed by a second shear crack with a mark in between being interpreted to be an arrest event (# 956 and # 957). In one case, # 962, the specimen did not follow one of these laws. It fractured under tension with an angle of about 50° but opposite to the expected 70° into the pressure field. An explanation for this behaviour (e.g. by bending during catching) is not available, since this fracture occurred at an early time as is shown by the photograph. In shot # 964 a finite shear crack length could not be determined because the crack did not stop in the specimen.

The tensile cracks show the typical characteristics. The surface is dull and rough and exhibits the usual "river pattern" produced by crack extension (see Fig. 14). The fracture surfaces show shear lips i.e. the edges are inclined at an angle of about 45° with respect to the plane middle part of the fracture surface).

The new phenomenon "dynamic shear fracture" does not only differ in the propagation direction from the 70° tensile fractures and from the tensile cracks which succeed the shear cracks, but also the appearance is principally different. The fracture surfaces of the straight propagating shear cracks do not show shear lips. The flat fracture surface extends over the total thickness of the specimen. The surface is not rough but shiny. Many isolated areas of the surface have a mirror-like appearance. A gliding process during the separation phase could have generated these surfaces. Melting temperatures may have occured at the surface.

The test parameters, the observed experimental findings, and data of evaluation procedures (which are explained later) are presented in Table 2. For an attempt to cast the experimental data of Table 2 into one diagram the following arguments were found:

(1) The data suggest the existence of a threshold velocity v_{th} for the formation of dynamic shear cracks.

(2) According to theoretical results of fracture mechanics (see for instance [3]) this threshold should be proportional to the square root of the notch tip radius:

$$v_{th} = \left(\frac{v_{th}}{\sqrt{\rho}}\right)_o \sqrt{\rho} \ .$$

(3) The shear crack length does not depend on the notch tip radius. From this follows that different but parallel curves will fit the results of specimens with different notch tip radii.

(4) The presumption that the dynamic shear crack length depends on the impact energy, i.e. on the square of the impact velocity, was not sustained by the experimental data. The data rather suggest a proportionality between impact velocity and shear crack length.

Consequently, an impact velocity versus shear crack length diagram has been drawn (Fig. 15). For a better distinction different symbols have been used for different notch tip radii. A computer fit was made with the data of the open circles (fatigue cracks) to find the slope of the parallel lines of the data with different notch tip radii. The threshold velocities are the intersection points with the horizontal axis and given numerically in Table 3. From the assumed proportionality between threshold velocity and square root of notch tip radius also the missing foot point for the line with ϱ = 0.75mm can be calculated as well as the effective radius of the fatigue data (0.15mm). The extrapolation of this line yields a fictive shear crack length of 68mm for shot # 964. Two data points do not fit well into the diagram, # 957 and # 958. An inspection of the notch tips did not reveal the reason for this behaviour. It is, however, to expect that data points outside the material scatter band are located in the regime of smaller notch tip radii since imperfections of the notch tip should result in a smaller effective notch tip radius. The likelihood for these deviations should increase with increasing notch tip radius. For these two points an effective radius of about 0.35mm may be estimated from Fig. 15.

A second diagram, Fig. 16, is drawn with the horizontal axis normalized by the square root of the notch tip radius. In this case a bunch of lines is to be expected with a sole common point which is the foot point on the horizontal axis. This concentration into one point is also an indication for correct determined threshold values in Fig. 15. The transformation of the lines from Fig. 15 into this diagram is mirror-like: the line with the fatigue cracks appears on the right side. The displacement of the two data points which do not fit into the diagram becomes even more obvious by this mathematical transformation. The calculation of the new position with a more suitable radius of e.g. 0.35mm would have placed them considerably better.

The arguments (1) to (4) given above and the experimental data make clear that a single curve for these results cannot be expected. The diagrams of Figs. 15 and 16, therefore, replace Fig. 12 of the interim report [12].

#	Test Parameters B mm	v_o m/s	ρ mm	a_s mm	Results fracture mode 1. crack	2.crack
913	9.3	19.8	f	4	shear + tensile	
914	9.3	31.9	a	30	shear + tensile	
916	7.9	31.7	t	26	shear + tensile	
918	9.4	32.0	i	20	shear + tensile	
919	8.6	30.3	g	20	shear + tensile	
964	19.0	54.3	u	>60	all shear	
965	19.0	32.1	e	31.5	shear + tensile	
915	8.4	32.5	0.25	17	shear + tensile	
960	19.0	29.8	0.30	5	shear + tensile	
961	19.0	38.2	0.30	31	shear + tensile	
920	8.8	32.4	0.35	12.5	shear + tensile	
921	8.5	50.7	0.35	47	shear + tensile	
962	19.4	22.4	0.35	-	tensile	
908	8.2	12.0	0.75	-	no fracture	
909	8.2	12.7	0.75	-	no fracture	
910	8.9	12.9	0.75	-	no fracture	
911	8.9	12.8	0.75	-	no fracture	
912	8.9	32.5	0.75	-	70° tensile	
955	18.8	39.9	0.85	0.5	70° tensile	
956	19.0	71.8	0.85	47	shear + shear	
957	19.1	50.8	0.85	42	shear + shear	
958	18.9	34.1	0.85	13	shear + tensile	
959	18.8	27.3	0.85	-	70° tensile	

List of symbols:

# = shot number
B = specimen thickness
v_o = impact velocity
ρ = notch tip radius
a_s = length of dynamic shear crack

Table 2 Data of shear experiments with steel specimens and experimental findings

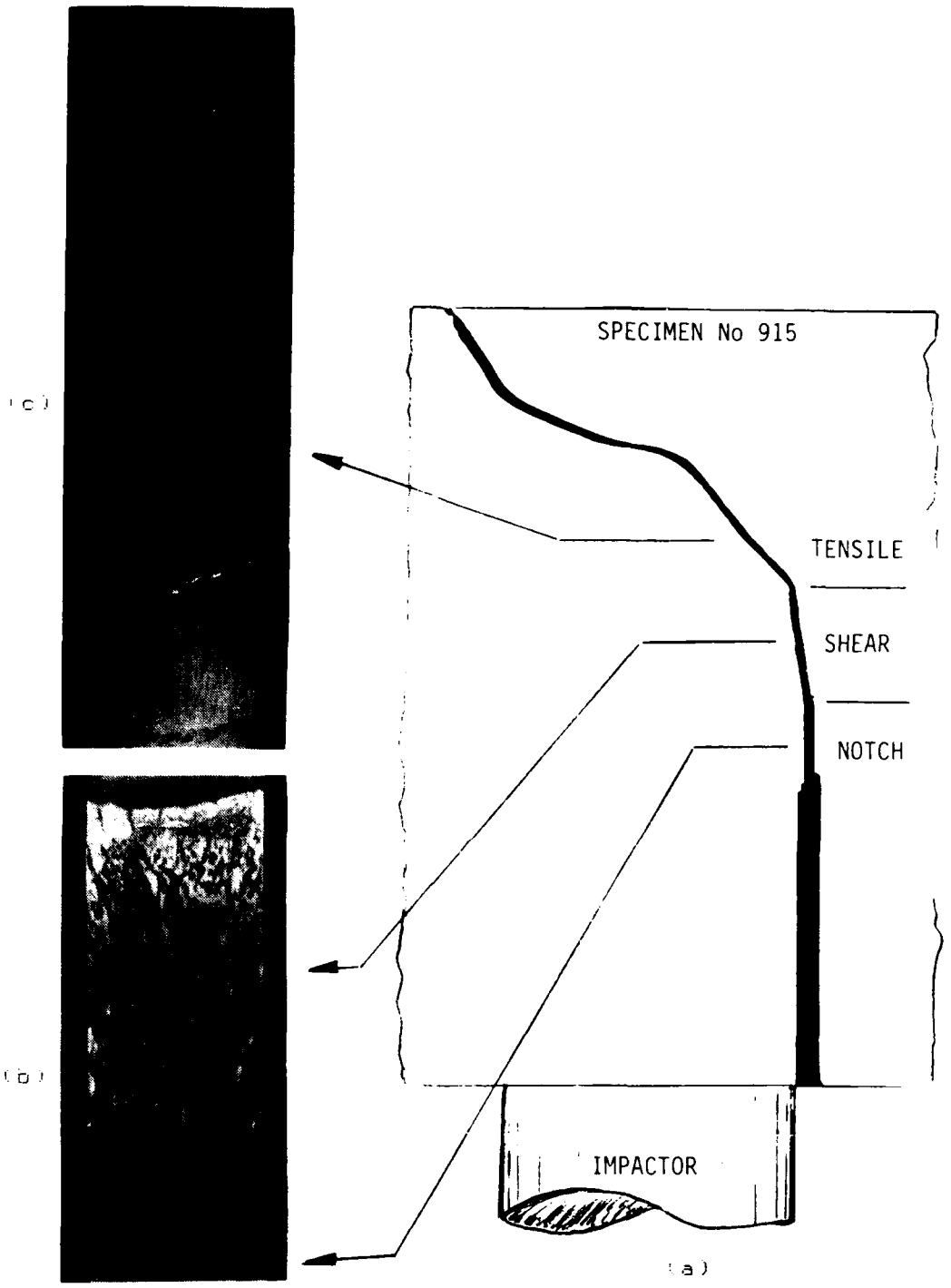

Fig. 14 Fracture surface appearance: (a) fracture path (b) shear fracture (c) tensile fracture, (# 915)

#	Test Parameters B mm	v_o m/s	Q mm	a_s mm	Results $v_o/\sqrt{Q}$ $\sqrt{m}$/s	v_{th} m/s	$v_{th}/\sqrt{Q}$ $\sqrt{m}$/s	symb
913	9.3	19.8	f	4	1 617	18	1 470	○
914	9.3	21.9	s	30	2 605			
916	7.9	31.7	t	26	2 588			
918	9.4	32.0	i	20	2 613			
919	8.6	30.3	g	20	2 474			
964	19.0	54.3	u	60	4 434			
965	19.0	32.1	e	31.5	2 621			
915	8.4	32.5	0.25	17	2 055	23	1 455	●
960	19.0	29.8	0.30	5	1 721	25	1 443	△
961	19.0	38.2	0.30	31	2 205			
920	8.8	32.4	0.35	12.5	1 732	27	1 497	▲
921	8.5	50.7	0.35	37	2 710			
962	19.4	22.4	0.35	-	1 197			
908	8.2	12.0	0.75	-	438	--	- ---	□
909	8.2	12.7	0.75	-	464			
910	8.9	12.9	0.75	-	471			
911	8.9	12.8	0.75	-	467			
912	8.9	32.5	0.75	-	1 187	(40)	(461)	
955	18.8	39.9	0.85	0.5	1 369	43	1 475	■
956	19.0	71.8	0.85	47	2 463			
957	19.1	50.8	0.85	42	1 742			
958	18.9	34.1	0.85	13	1 170			
959	18.8	27.3	0.85	-	936			

mean value: 1 468±21

List of symbols:

# = shot number
B = specimen thickness
v_o = impact velocity
v_{th} = threshold velocity
Q = notch tip radius
a_s = length of dynamic shear crack

Table 3 Data of shear experiments with steel specimens, results, and evaluations

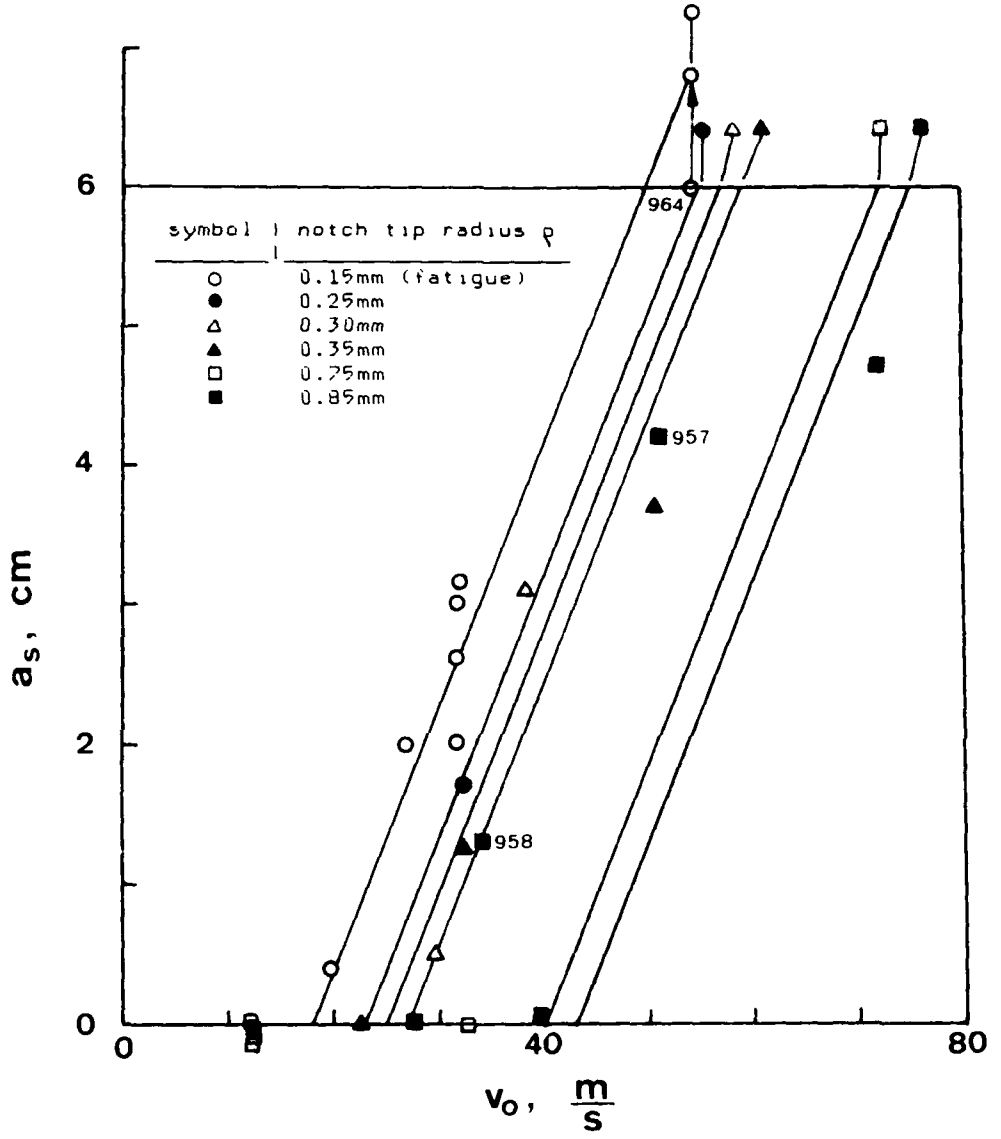

Fig. 15 Shear crack length as a function of impact velocity and of notch tip radius

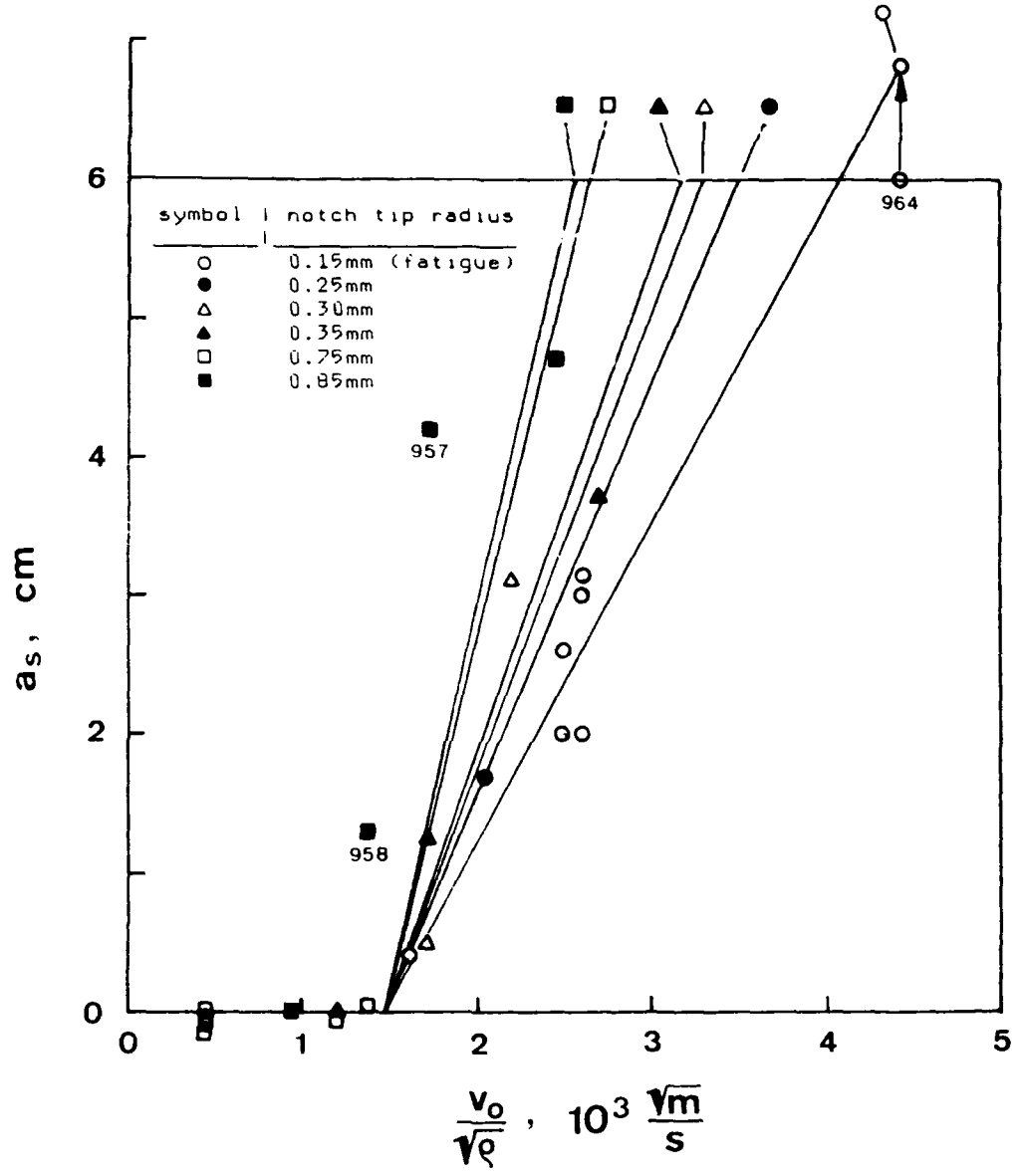

Fig. 16 Shear crack length as a function of impact velocity and of notch tip radius

3.2.4 Dynamic Shear Fracture Formation

The appearance of the crack surfaces of the high strength steel specimens suggests a glicing process between the upper and the lower surface during the crack generation phase. The shiny smeared-out regions are larger in size at the beginning of the crack near the notch and the dimples which have a circular configuration with the tensile fractures are elongated and parabolicly contoured. This is shown in the micrographs of Fig. 17 with a transition from shear fracture (lower left corner) to tensile fracture (upper right side) showing the change in the formation of the dimples from the parabolic to the circular shape.

This sort of "dynamic shear fracture" could, however, not be produced with other materials. Experiments have also been performed with the steels 38 NiCrMoV 73 (HF% 103), 42 CrMo 4, and the mild steel StE 460, all in a non-hardened state. Non of these specimens, although impacted with very high projectile velocities (up to 112 m/s), broke into parts. Only short shear cracks were produced, if any. Figs. 18 and 19 show an example with the material 42 CrMo 4 (# 929, impact velocity 102 m/s).

The impacted specimen original size 120mm * 78mm * 10mm) is shown in Fig. 18a with the notch on the left side and the impacted part clearly visible on the top (compression about 8 mm). Lines to identify positions have been traced on the surface before the test. The distance of the narrow lines in the undisturbed material is 2.5 mm. The first one of these narrow lines from the top indicates the original notch tip position (tip radius 0.2mm). Fig 18b is a magnification of this area.

A photomicrograph of the sheared part of this specimen is Fig. 19. The length of the crack shown in Fig. 19a is about 7.5mm. Fig. 19b is a detail of this crack. The peculiarities of these pictures are white bands on both sides of the crack and also white fragments inside the crack. These white parts became visible by etching the sample *) and are known in the literatur as adiabatic shear bands.

Adiabatic shear bands are produced in a small volume of very high shear strain gradient by heating up to almost melting temperatures and a hardening process during a succeeding rapid cooling. The width of the band is of the order 0.01mm and of little mass only, where the material is transformed into a martensitic state. Rapid cooling of the small band volume is achieved by the two large interfaces to the cold bulk material.

---

*) Etching agent: 3% Nital

The hardness distribution across the shear band is almost rectangular as shown in Fig. 20. This profile shows an increase in the microhardness HV 0.025 in the band by almost a factor of three compared to the bulk material which is heavily plastically deformed and, therefore, also shows an increased hardness compared to the base material.

Shear bands have not be found in the other materials, especially not in the maraging steel specimens of section 3.2.3 where "dynamic fractures" have been observed. In this type of steels martensitic hardening is not possible and separation may have occurred instead in the weakend microstructure or even in the liquid state at the tip of the fast moving shear strain concentration. The heat conduction of this material is known to be up to 10 times lower than in ferritic steels. Then the heat generated at the crack tip remains much more concentrated in the maraging steel whereas it dissipates fast in the others. This could explain that the observed shear fracture phenomena were found in this material only.

Ferritic materials with a relatively low yield strength, on the other hand, may not develop a shear strain concentration sufficiently high to form a heat source capable for inducing material transformations. This is a consequence of the front of the compressive wave not being a step function. Since the material starts yielding at a low level a high strain gradient cannot develop and there is sufficient time for the material to flow away during the long period of increasing pressure. With this material only very high impact velocities are expected to produce shock waves with strain concentrations sufficiently high to generate shear bands.

The consequence of these observations is that the phenomenon of "dynamic shear fracture" has to be described by different processes in different materials. To break a shear band like the one in the ferritic steel of Fig. 19 will probably need only little energy, because the transformed material is very brittle. This crack does not look like a shear crack. It may have been produced after cooling down of the band material not under shear load but due to residual tensile stresses generated in the bulk material during the cooling process. A tensile loading of the shear band could also have been produced by a compression of the notch surfaces due to the lateral material expansion in the compression pulse. There is some indication of this in Fig. 18. This hypothesis is supported by the finding that many unbroken shear bands were found at places where these sort of load may not have been available.

Shear fractures were also found in some of the projectiles used to impact the plate specimens. The projectiles were fabricated from the steel 42 CrMo 4 and induction hardened. At the edges of the indentations formed by the impact (see sketch in Fig. 21a) large shear cracks were formed. Some of them have been investigated metallographically. These cracks are much larger due to the increased hardness of the material and show also all interesting features. Fig. 21a is a sketch of the impacting part of a projectile (shot # 925) and Fig.21b shows an over all view of a compressed edge with a large shear crack. Fig. 21c, finally, is the magnified area of the very beginning of the crack showing an array of shear bands 10 to 30 mikrometres in width. Figs. 22 to 25 show microphotographs of the etched material: sometimes the crack has extended in the white shear bands and is even filled with fragments of the transformed material (Fig. 22 and 23). Fig. 24, however, shows the end of the crack which was not preceded by a shear band. Fig. 25 shows an area very close to the edge of the indentation with an unbroken shear band.

Photomicrographs (light and scanning electron microscope, LM and SEM) of another sectioned projectile (shot # 929) are shown in Figs. 26 to 28 indicating the rather abrupt transition between the adiabatic shear band and the surrounding material. Etching of the white band, i.e. the transformed material, is less easy than with the surrounding material. The SEM micrographs suggest this material being raised over the surrounding material. Obviously, the white band is very hard, which is in agreement to Fig. 20. The light microscope does not resolve the microstructure of the band which is believed to be martensitic. Details must be smaller than one micrometre. Also the surrounding material is strongly deformed by shearing. Even damage can be seen in this material (Fig. 27). The toughness of this material seems to be reduced. The drop of toughness in the shear band in combination with residual stresses in the specimen possibly often leads to fractures within the band (Figs. 27 and 28).

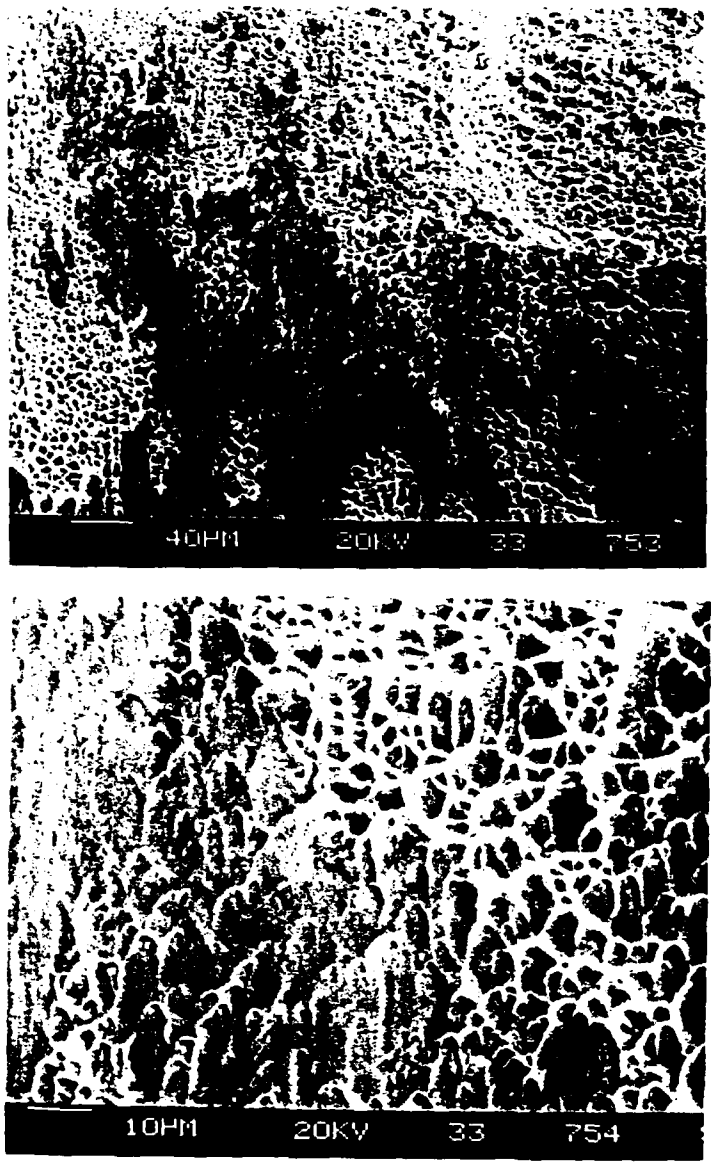

Fig. 17 Fracture surface in different magnifications, transition from shear (lower left corner) to tensile fracture (upper right corner); SEM microphotograph (shot # 916); the lower picture is a detail from the center of the upper

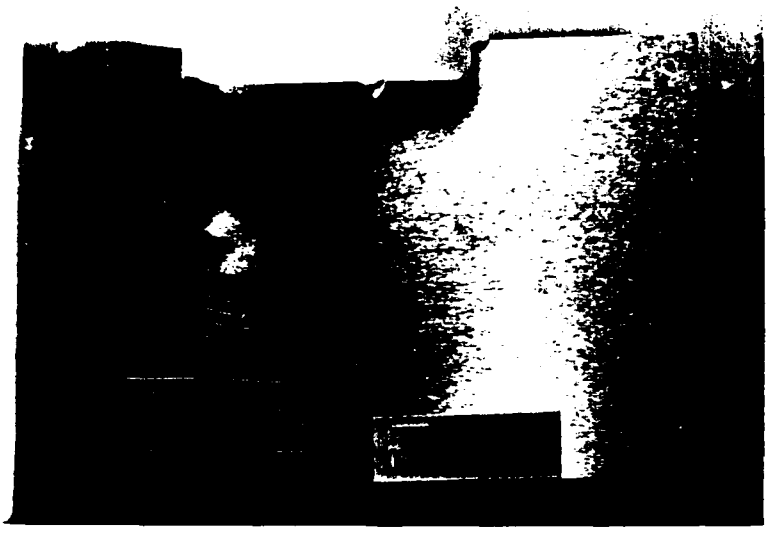

(a)

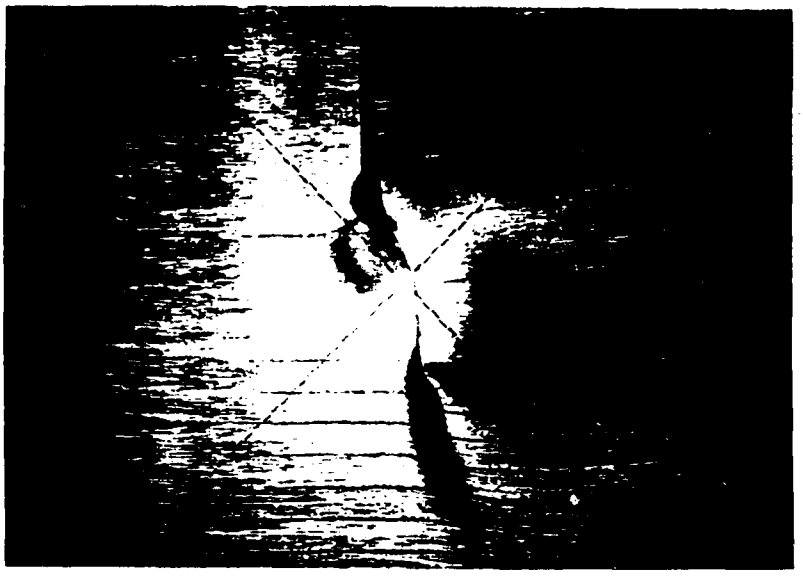

Fig. 18 Specimen of shot # 929, 42 CrMo 4, impacted at 102m/s; (a) over all view, (b) detail

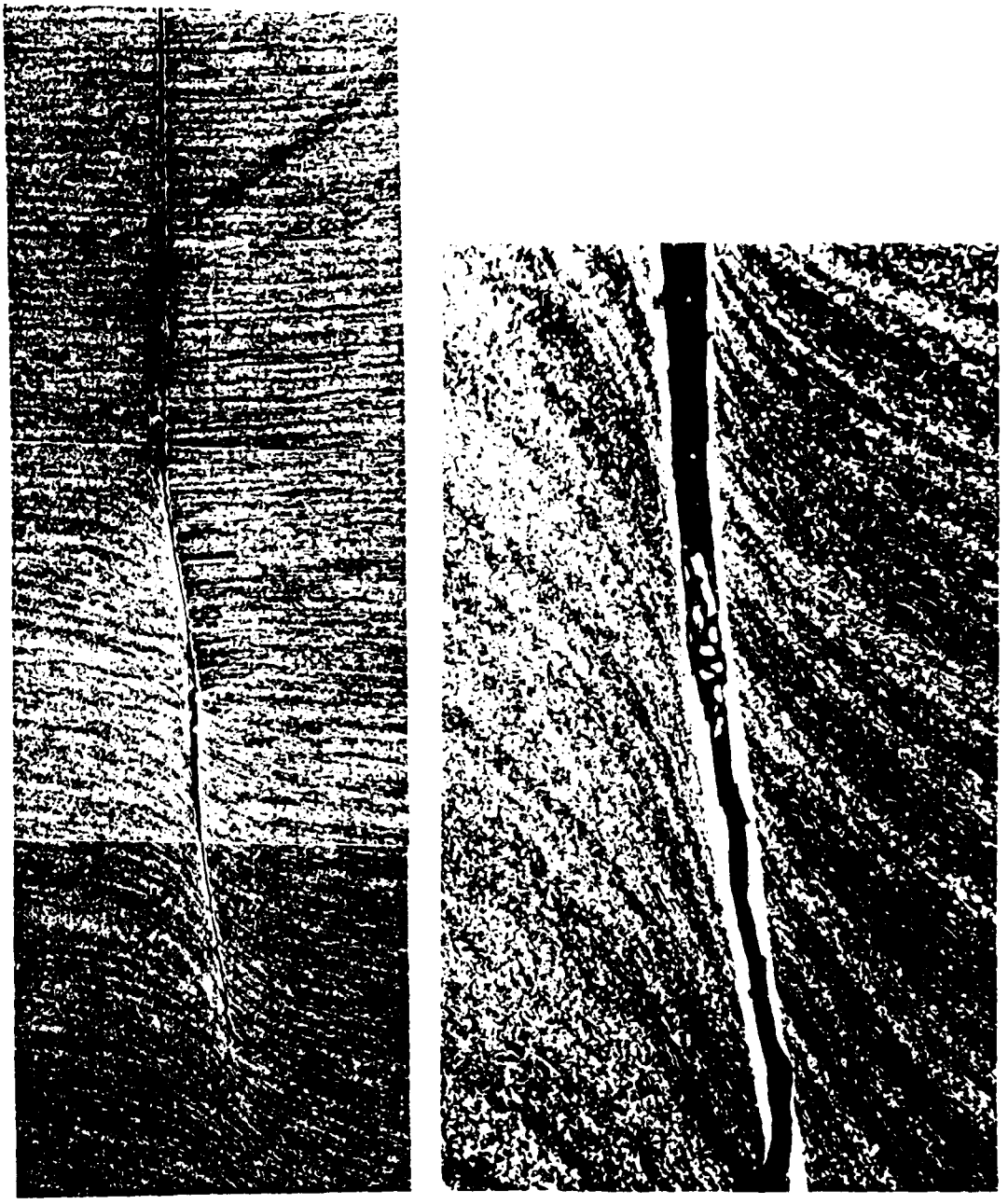

Fig. 19 Crack at notch tip (shot # 929), (a) over all view (length of the visible crack ~ 2.5mm), (b) detail

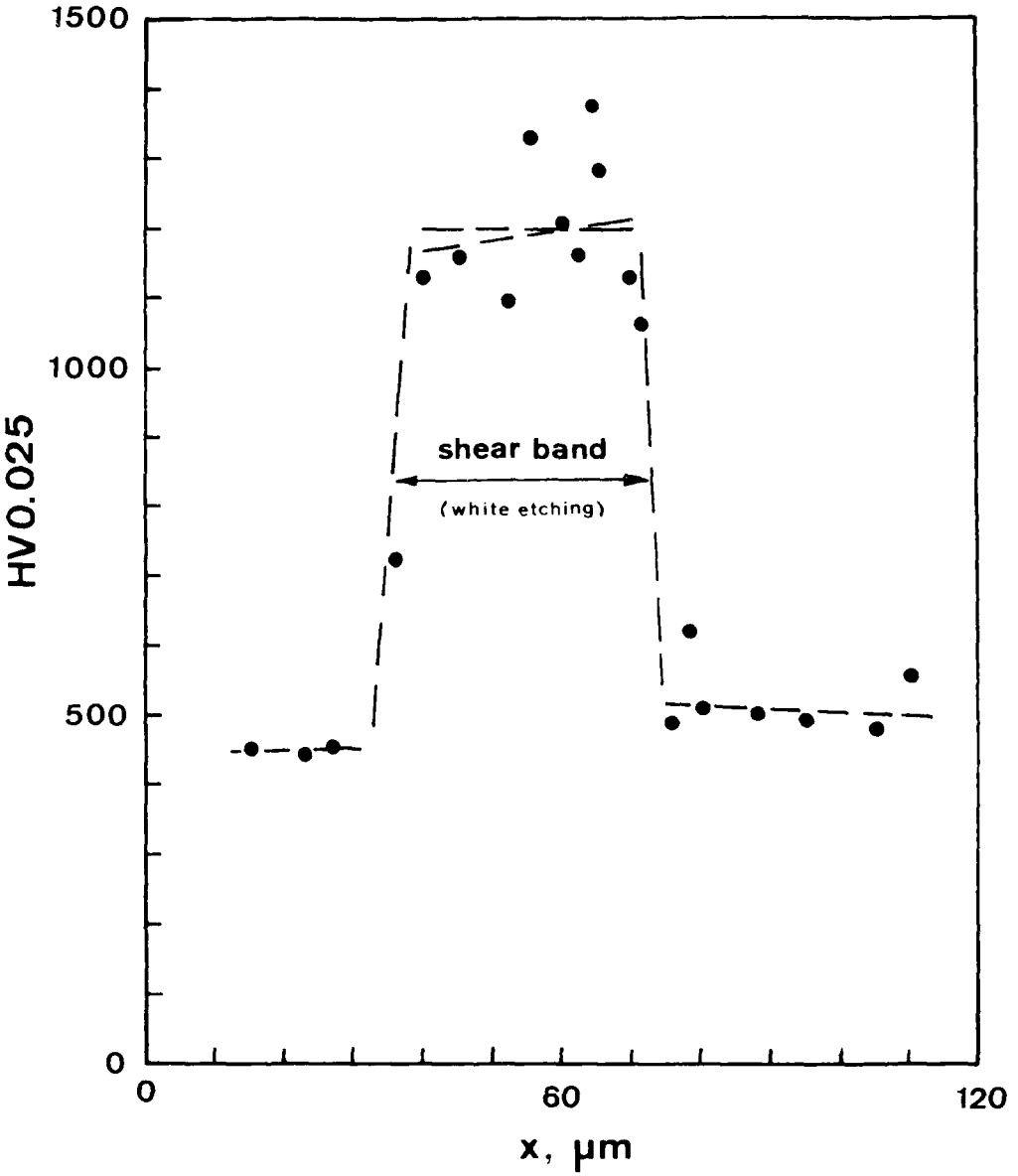

Fig. 20 Hardness profile across an unbroken adiabatic shear band of Fig. 21c (# 925, projectile)

(a)

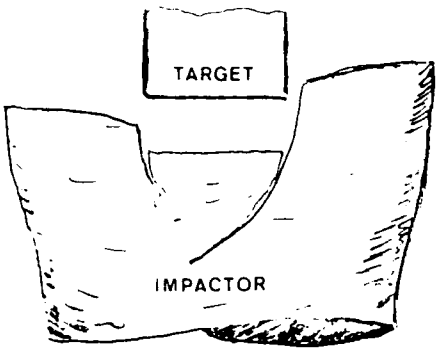

(b)

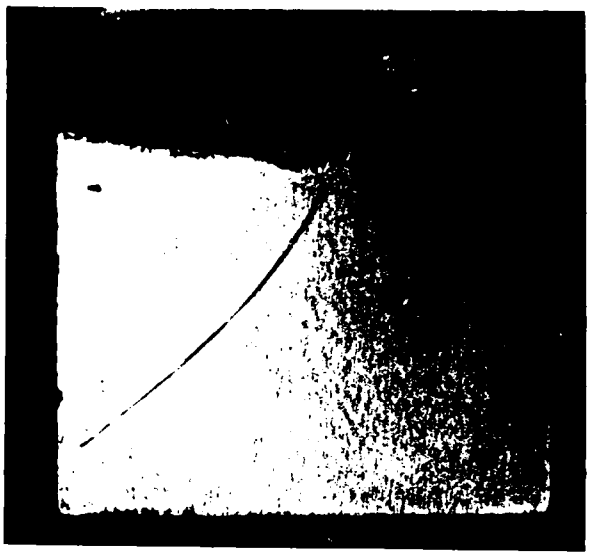

(c)

Fig. 21 Projectile indentation (# 925), (a) sketch of the impact area, (b) over all view of one sheared edge (c) broken and unbroken shear bands at the edge

Fig. 22 Projectile indentation (# 925): sheared material, crack with shear band

Fig. 23 Projectile indentation (# 925): detail of broken shear band with fragments of transformed material

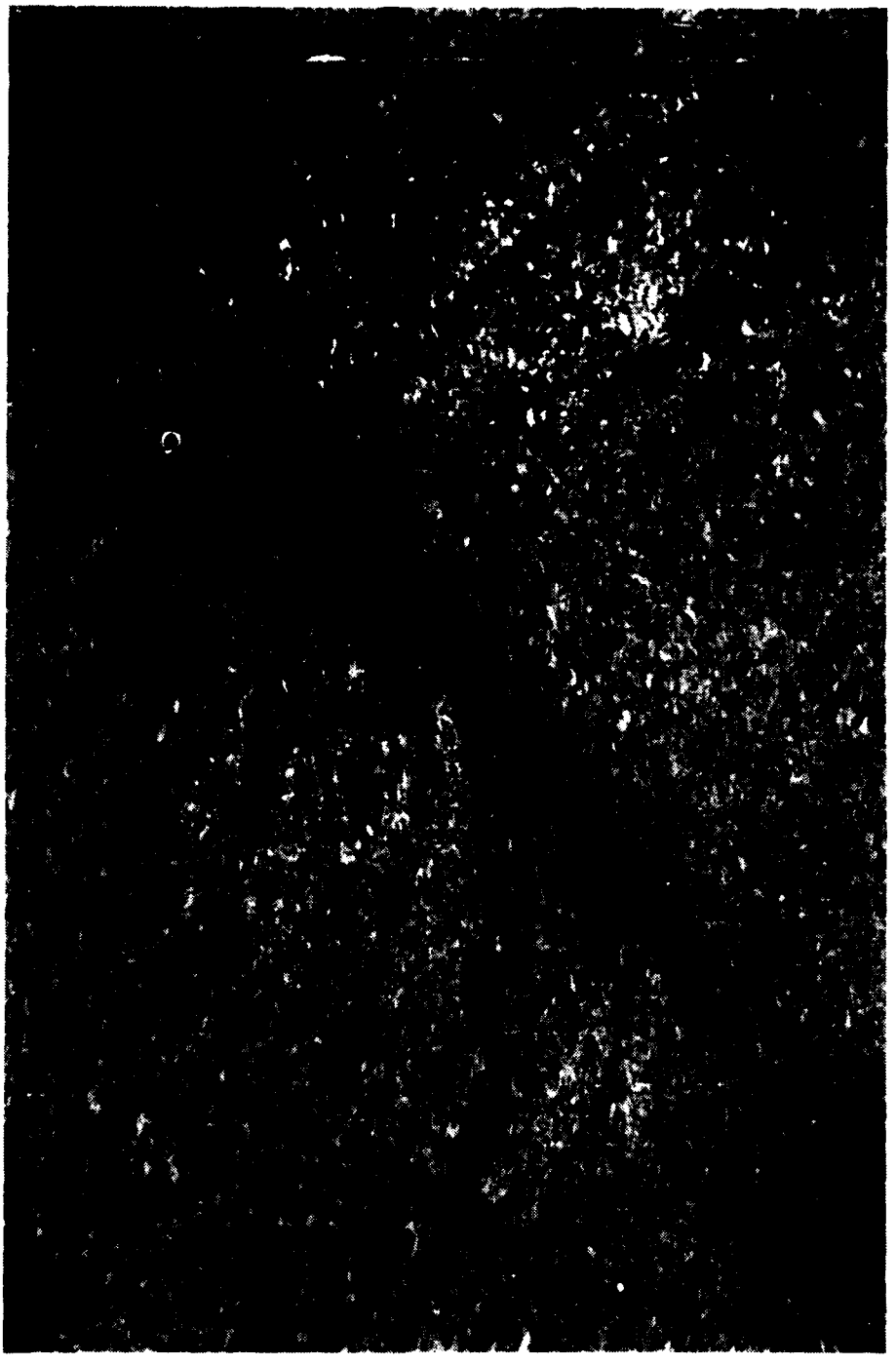

Fig. 24 Projectile indentation (# 925): crack end

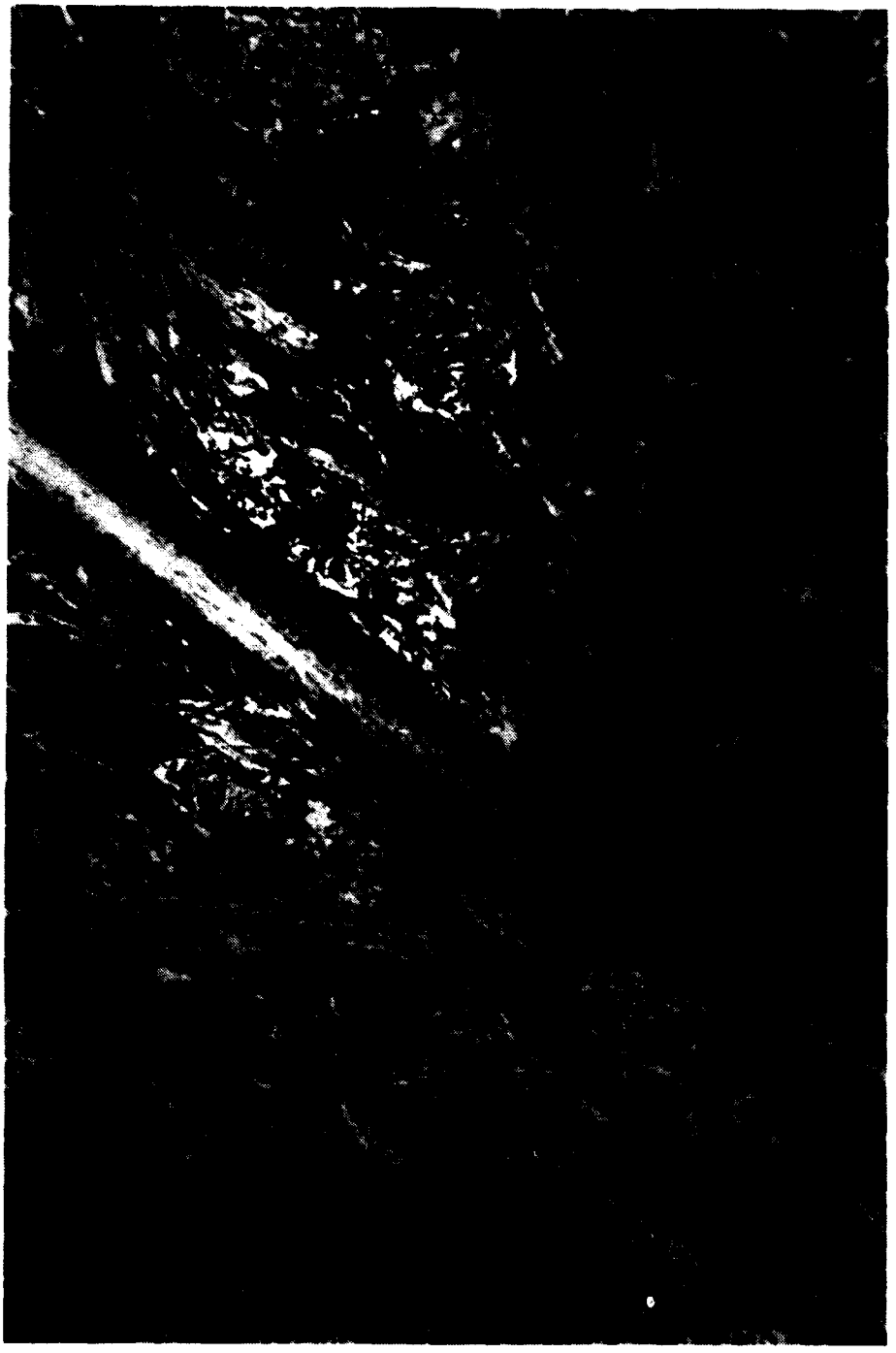

Fig. 25 Projectile indentation (# 925): unbroken shear band near edge

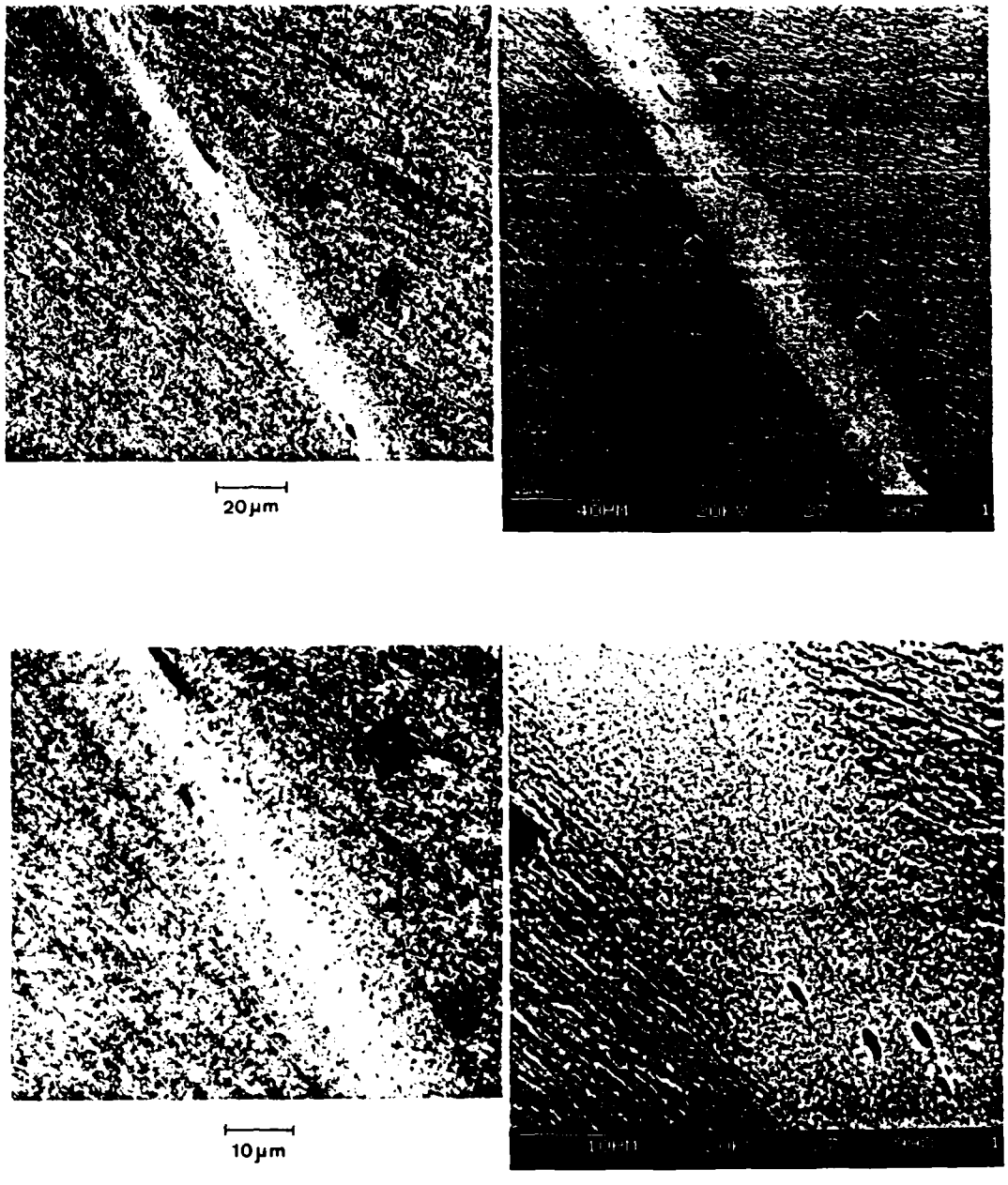

LM (SEM, material contrast)

Fig. 26 Shear band in projectile (# 929), unbroken, different magnifications

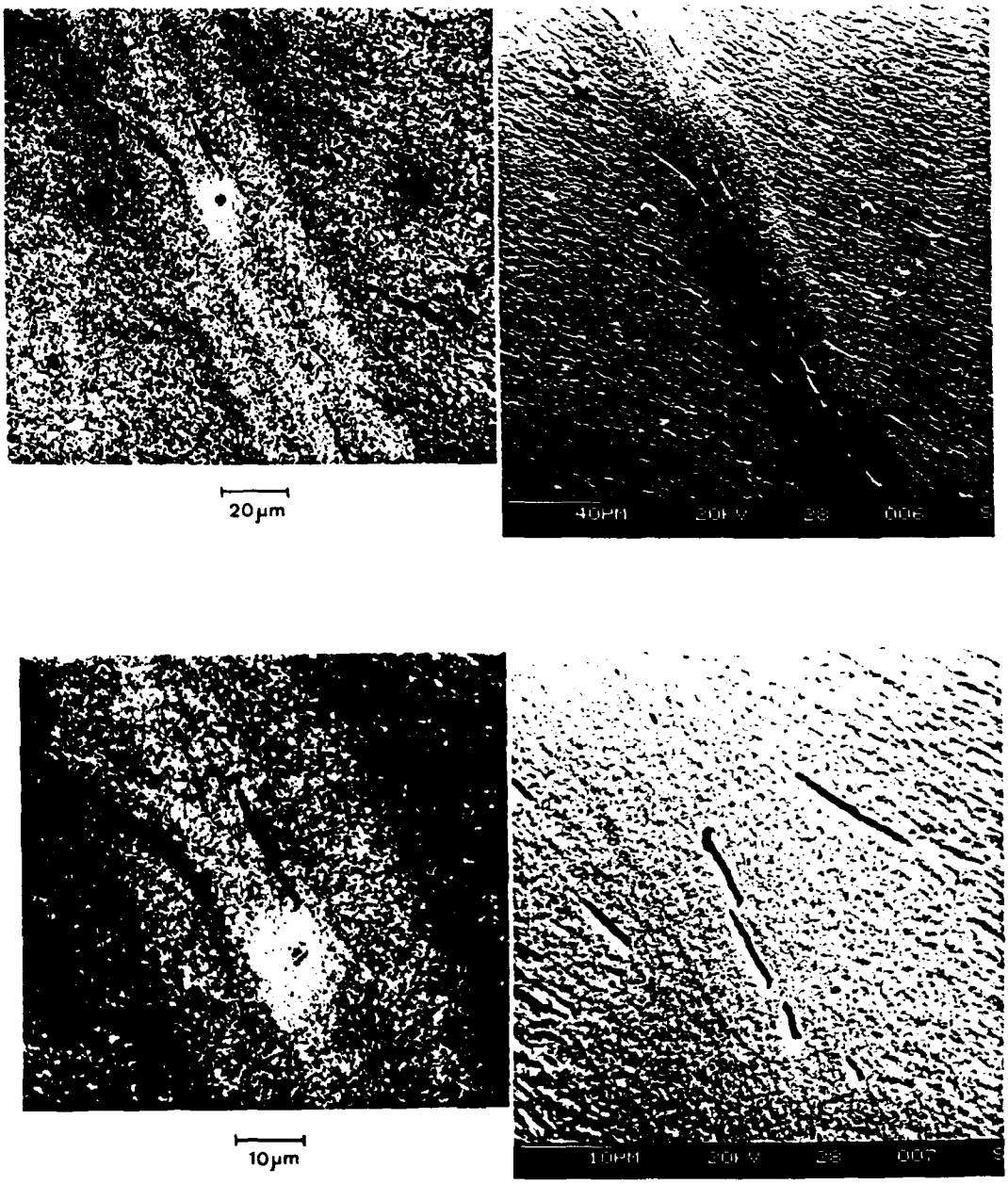

LM (SEM)

Fig. 27 Shear band in projectile (# 929), beginning of damage, different magnifications

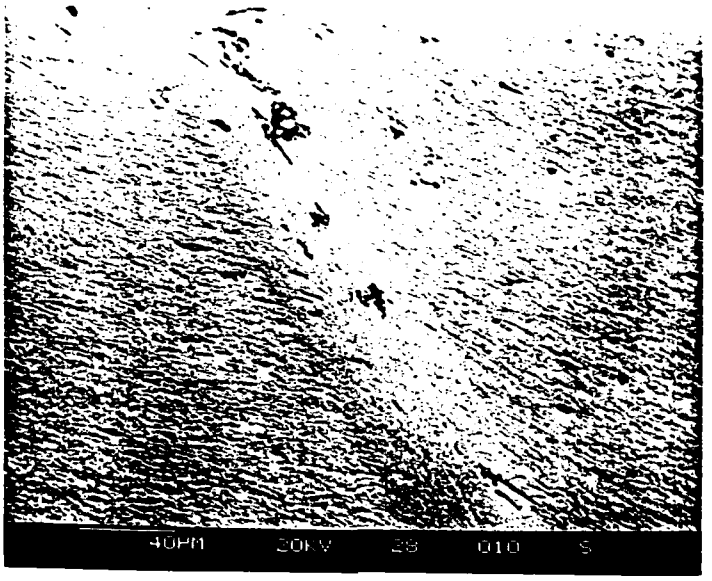

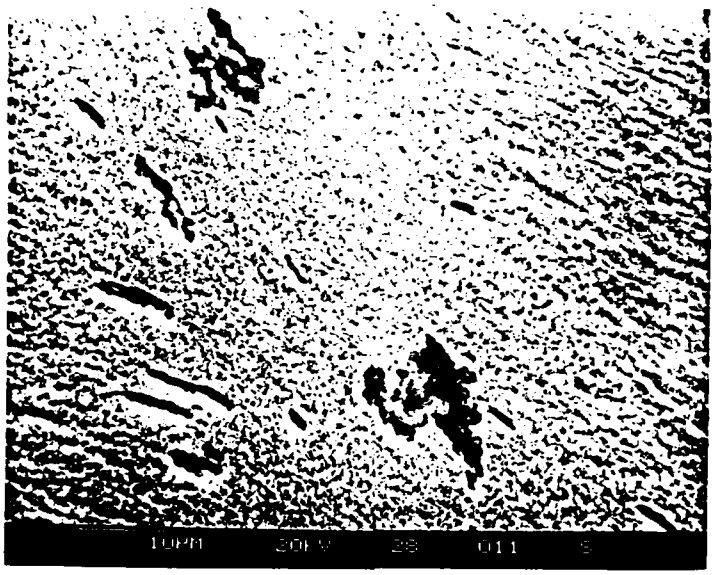

Fig. 28 Shear band in projectile (# 929), broken, different magnifications (SEM)

4. WORK ON RESEARCH TASK 3: CRACK PROPAGATION UNDER THE PHASE OF PRIMARY COMPRESSION

K-measurements under direct impact loading conditions performed within the previous contract could not be carried out with Araldite B specimens for impact velocities $v_0 > 50$ m/s because the cracks already became unstable during the phase of compressive load and propagated in a direction perpendicular to the original crack orientation. Obviously, tensile stresses are produced during this early phase by lateral expansion when the compression pulse traverses the specimen. An investigation of this phenomenon has been conducted using specimens with cracks positioned parallel to the impact direction as is shown in Fig. 29.

Two series of experiments using specimens fabricated out of Araldite B were performed in which the geometry of the test specimens was varied to get information on the parameters which might control the loading rate. In the first series of experiments the height h of the specimen was varied from h = 55mm, h = 75mm, h = 100mm, up to h = 150mm. In the second series of experiments the length of the center crack was varied from 2a = 20mm, 2a = 30mm, to 2a = 60mm. The length L of the specimen was kept constant throughout all the experiments, L = 400mm. The specimen dimensions are given in Fig. 30. The specimens were impacted at a velocity v_0 = 52 m/s by a steel projectile. The test conditions are given in Table 4. Again the shadow optical method of caustics was used to investigate the crack tip loading.

A typical series of shadow optical photographs is shown in Fig. 31. Compressive caustics are observed first at both crack tips when the compressive stress pulse propagates along the crack. This causes crack closure which generates the observed compressive crack tip caustics. Later on, the compressive crack tip caustics rapidly change into tensile crack tip caustics. This process takes place earlier and more gradually for the left (the tip first hit by the pulse front) than for the right crack tip. The steep increase in size of the right tensile shadow spots was the reason for hoping that very large crack tip stress intensification rates could be produced by this method.

Quantitative results for a specific geometry (shot # 930) are given in Fig. 32. Time counting was started when with the left crack tip the pressure caustic changed into a tensile caustic. From this instant tensile loading of the left crack tip (x = -a) is observed. Tensile loading of the right crack tip (x = +a) is about 12 µs delayed. The increase of this second stress intensity factor curve, however, is considerably steeper than that of the first one.

The achieved crack tip stress intensification rates dK/dt for the performed experiments are summarized in Table 4. Graphical presentations of the loading rates obtained for the right crack tip are shown in Fig. 34 as a function of the height of the specimen and in Fig. 35 as a function of crack length: Increasing rates of the stress intensification factor K are obtained when the height of the specimens is decreased. It is concluded, therefore, that the reflection of waves at the upper and lower boundary of the specimen will cause this effect. An explanation is tried with the aid of Fig. 33:

According to Hooke's law lateral stresses behind the front of the compressive wave are $\sigma_x \cdot \nu/(1-\nu)$ (about 0.9 times the stress in propagation direction). The components which are directed normal to the crack tend to close it. Consequently, pressure shadow patterns are observed at both tips during this first loading period. The front of the compressive longitudinal wave produces also shear waves at the upper and lower boundaries of the specimen (see Fig. 33) to meet the condition of zero normal stresses at the free surfaces. These two shear waves propagate into the specimen and superimpose in the center plane, the plane which contains the crack (Fig. 36). The crack is hit first by this wave combination at the left tip $x = -a$ with $\tan \alpha = c_T/c_L$, where c_T and c_L are the propagation velocities of transverse and longitudinal waves, respectively. The normal-to-the-crack components of the two shear waves form a tensile loading of the crack turning first the pressure caustic at the $x = -a$ tip into a tensile caustic. This tensile loading, however, is hindered in its development by the fact that for a certain time the rest of the crack remains under pressure. This time can be calculated to $2a/c_L$ (Fig. 33). In the experiment of Fig. 32 a time shift of 12.5 µs is calculated and also observed for the onset of a tensile shadow pattern at the $x = +a$ tip (dark line in Fig. 32).

The resulting rates of stress intensification given in Table 3 are compared in Fig. 36 with results of the previous contract ([1], Fig. 38) for direct impact loading. The values of Table 4 can be averaged because the impact velocity was constant 52 m/s with all tests. One point, therefore, represents all data for the crack tip $x = -a$ (open circle) and another one (full circle) is the mean value for the $x = +a$ crack tip, the interesting one. For one shot, # 946, the data for the left tip is extremely high which seems to be unrealistic. A second mean value has, therefore, been calculated with this data not taken into account. This is given in Table 4 and in Fig. 36 (dashed circle) because it might better represent reality. The increase in stress intensification must be considerably handicaped by the stress closing the remainder of the crack and should,

therefore, be smaller than the previous values. The interesting result of these investigations is demonstrated by the black dot in the diagram (Fig. 36) showing that the rate of the stress intensification is increased by more than a factor of 2 with this method of unloading a compressed crack by a shear wave combination. These experimental findings show what was expected by the drawing of Fig. 33.

From Fig. 33 it is also obvious that the crack length does not have an influence on the rate dK/dt which is verified by Fig. 34. Increasing this measure just shifts the x = +a curve to the right (Fig. 32). An influence of the width h on the rate dK/dt which was measured with this program (Fig. 35) may be due to a reduced energy density in the specimen with increasing width (i.e. increasing volume). This reduces the rise time of the stress pulse and consequently also the rise time of the shear waves which directly determines dK/dt. These shear waves are also rarefaction fans with rise times depending on propagation distance. It must, therefore, be expected that with increasing height the rate dK/dt of the stress intensity factor decreases.

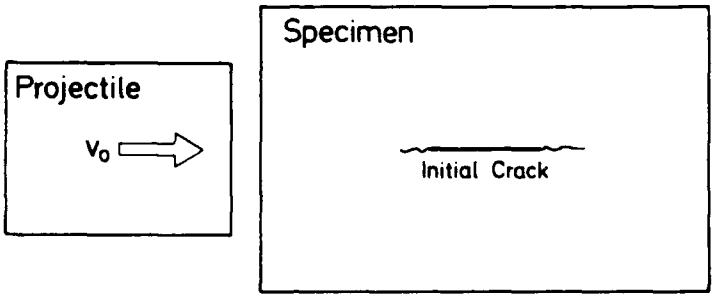

Fig. 29 Arrangement for fast tensile loading of cracks during pulse compressive loading (schematically)

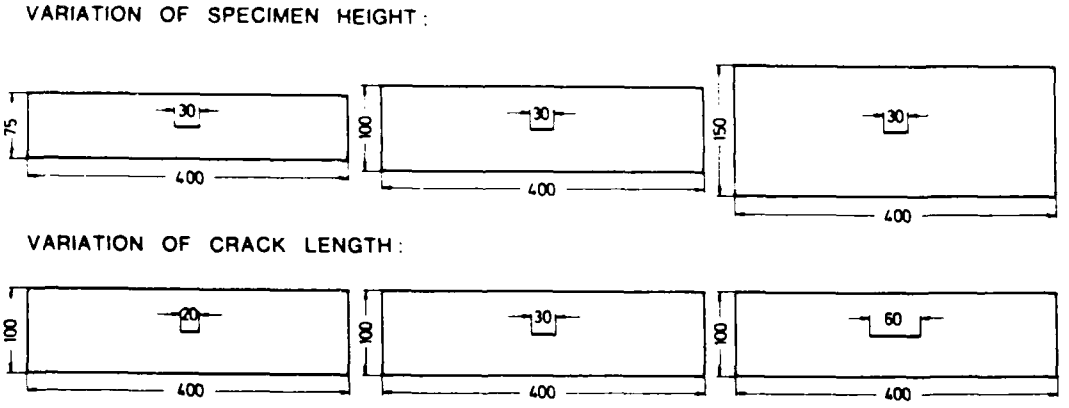

Fig. 30 Variations of specimen geometry

	Test Conditions			Results	
#	2a mm	h mm	v_o m/s	$\dot{K}$ (x=-a) MPa$\sqrt{m}$ /s *10^5	$\dot{K}$ (x=+a) MPa$\sqrt{m}$ /s *10^5
930	30	100	52.2	0.79	2.8
931	30	100	52.2	1.03	4.2
932	30	75	50.5	0.71	3.8
933	30	75	51.4	-	-
934	30	75	52.2	0.91	4.2
935	30	150	51.9	-	-
936	30	150	52.2	1.2	2.6
937	30	150	52.2	1.15	2.2
938	30	100	52.2	1.07	3.8
939	60	100	52.4	-	-
940	60	100	52.2	-	4.0
941	20	100	52.4	-	-
942	20	100	52.4	-	-
943	20	100	52.7	1.48	4.0
944	20	100	52.4	1.48	2.9
945	60	100	52.1	-	2.9
946	30	55	52.5	4.8	5.2
947	30	55	52.5	2.27	4.2
948	30	55	53.3	-	-
949	30	55	53.0	-	-
mean values:				1.5±1.2	3.6±0.8
(# 946 omitted:				1.2±0.5)	

(specimen length 400mm)

List of symbols:

#	shot number
2a	crack length
h	specimen height
v_o	impact velocity
$\dot{K}$	rate of stress intensity factor

Table 4 Test conditions and results of cracks loaded in tension by superimposing shear waves

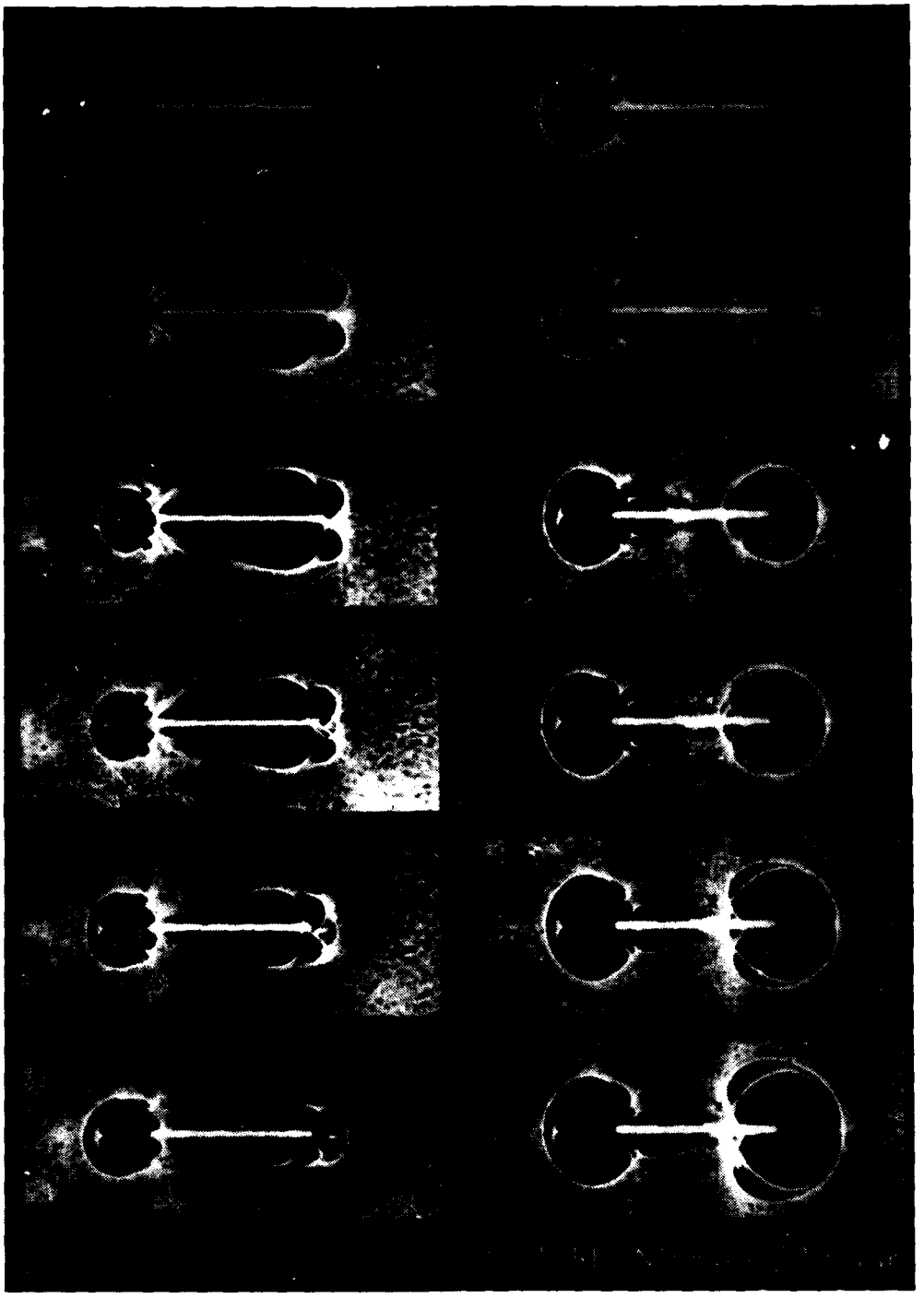

Fig. 31 High speed series of shadow optical photographs; crack tip stress intensifications during the phase of primary compression (Araldite B)

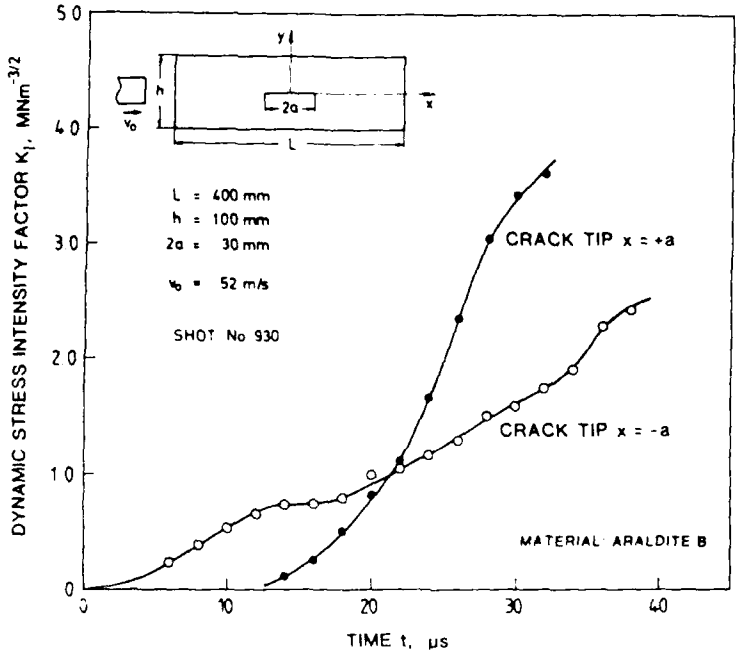

Fig. 32 Stress intensity factor at left (x = -a) and right (x = +a) crack tip during the phase of primary compression

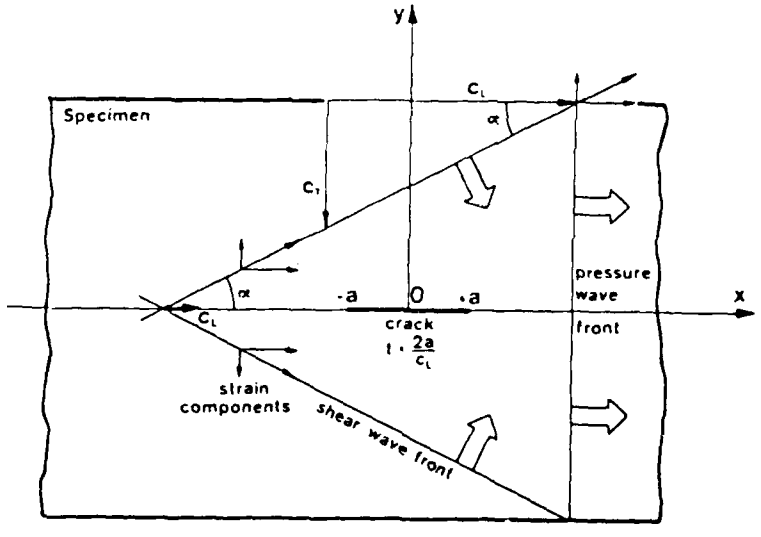

Fig. 33 Tensile loading of a crack by shear waves drawn at the specimen boundaries

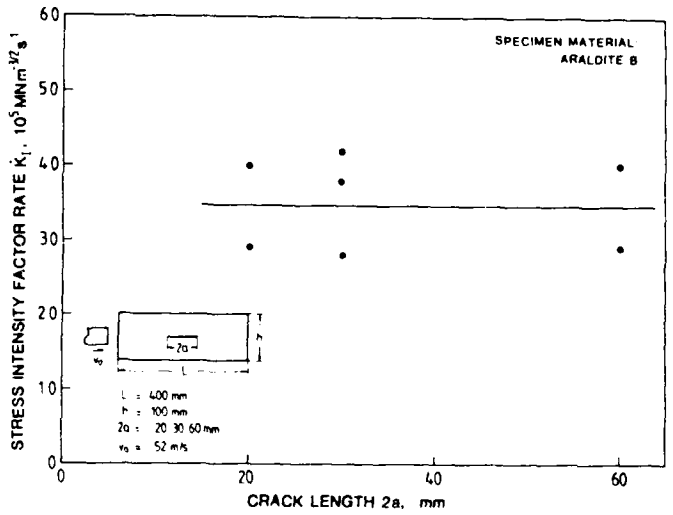

Fig. 34 Stress intensification rate dK/dt obtained for specimens with different crack lengths

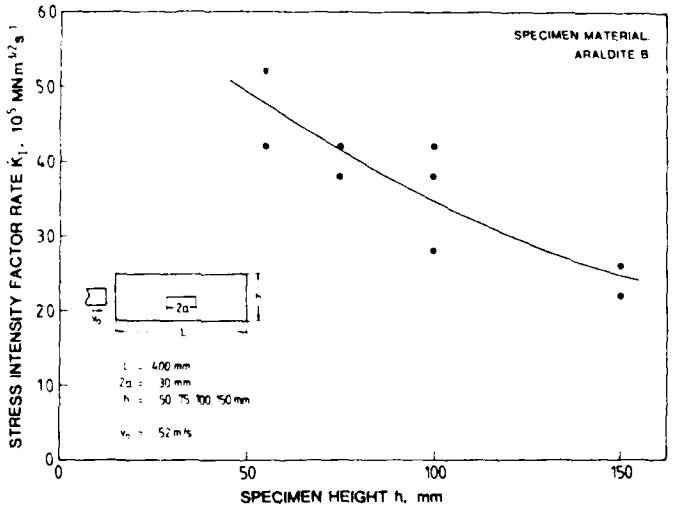

Fig. 35 Stress intensification rate dK/dt obtained with specimens of different height

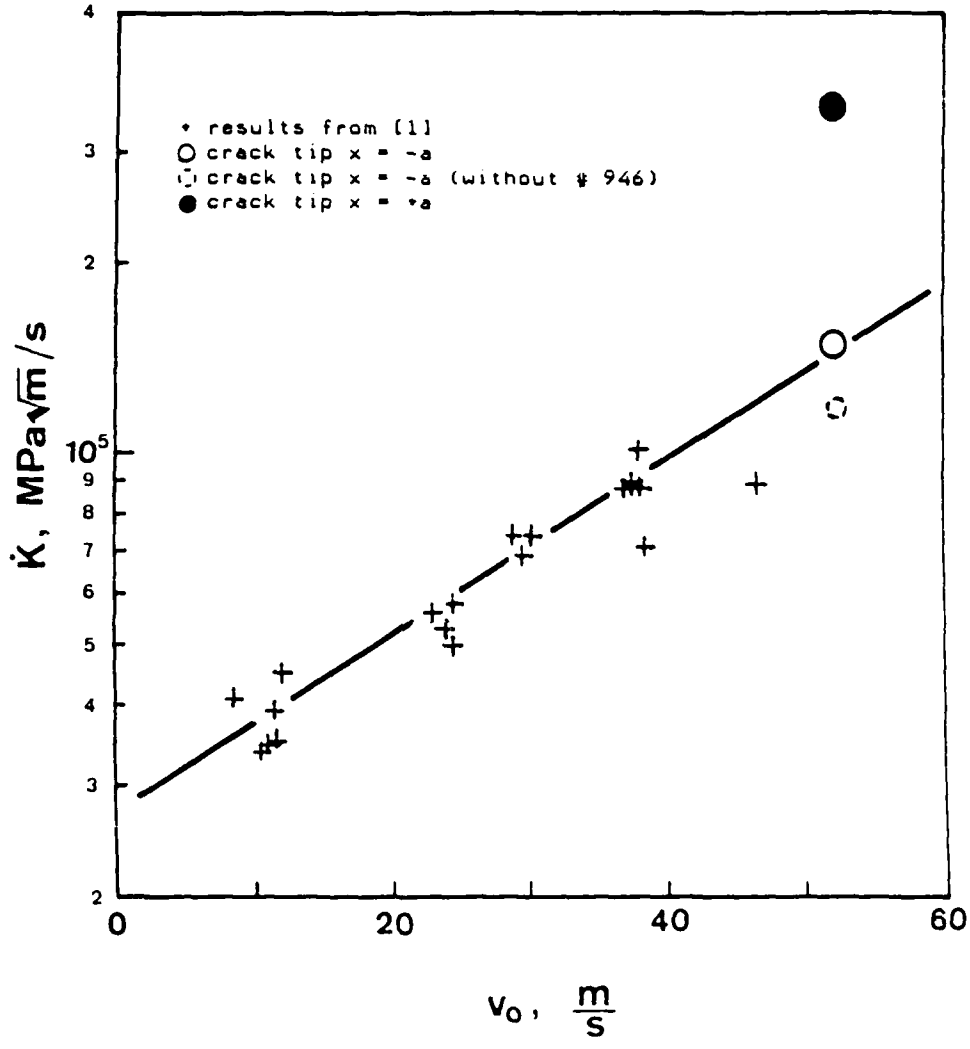

Fig. 36 Stress intensification rate dK/dt versus impact velocity; data of this contract compared with the data of the previous contract [1]

5. WORK ON RESEARCH TASK 4: IMPROVEMENT OF THE SHADOW OPTICAL METHOD IN REFLECTION

Within the previous contract shadow optical pictures have been photographed in reflection with high strength steel specimens impacted under direct loading conditions. These photographs showed disturbances due to surface waves. The larger the impact velocity and the larger the observation time the more severe were the observed disturbances (see Fig. 37). K measurements were limited to rather modest impact velocities. It has been proposed, therefore, to improve the procedure of photographing shadow optical pictures in reflection.

After a study of the shadow optical imaging process (for the shadow optical method see Appendix and [4]) and the sensitivity of the shadow optical effect resulting for different stress-strain concentration problems, a way was found to reduce the disturbances resulting from Rayleigh surface waves that an evaluation of crack tip shadow patterns at increased impact velocities becomes possible.

For illustration of the technical background on which this improvement is based, three stress-strain concentration problems with different stress gradients are considered (see [4] and Fig. 38):

(a) a circular hole subjected to bi-axial stresses p, q,
(b) a point load acting on a half-plate, and
(c) a crack under mode I tensile loading.

The curves $D(z_o)$, combining the size D of a characteristic measure in the reference plane (in the shadow pattern) with the distance z_o between specimen and this plane for these three problems are given by (see [4]):

$$D_i(z_o) = A_i \, m^{1-q} \, z^q \quad , \qquad \begin{array}{c|c|c|c} i & a & b & c \\ \hline q & 1/3 & 1/4 & 2/5 \end{array} \qquad (1)$$

$$m = \frac{Z - z_o}{Z}, \qquad Z = z_o + z_1 \qquad (2)$$

m is the magnification or scaling factor due to not parallel light. Z is the distance from light source to specimen and the factors A contain all constants of minor importance in this context. The geometrical relationships applied with this work are illustrated in Fig. 39. This is the case of

convergent light with m < 1.

For these three problems the resulting stresses vary with $1/r^2$, $1/r$ and $1/\sqrt{r}$, respectively, where r is the radial distance from the origin, defined in Fig. 38. In a shadow optical arrangement with convergent light beams the largest shadow patterns for these three stress-strain concentration

Fig. 37 Disturbances of shadow patterns obtained in reflection with steel specimens due to surface Rayleigh waves

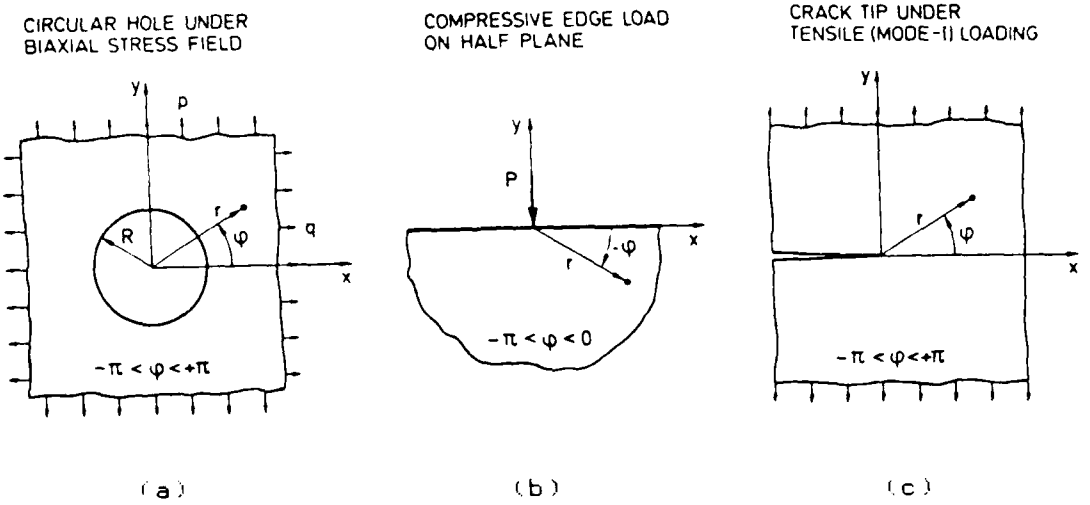

Fig. 38 Stress concentration problems of different stress singularities

problems are obtained for distances z_o between the specimen and the shadow optical image plane (reference plane) given by the relations

$$\begin{aligned} &(a) \quad z_o = 0.25\ Z \\ &(b) \quad z_o = 0.33\ Z \\ &(c) \quad z_o = 0.40\ Z. \end{aligned} \tag{3}$$

It can be deduced from this that in order to observe the largest possible shadow pattern the distance z_o of the reference plane from the specimen must be larger for the stress-strain concentration problem with the lower gradient. These relationships $D(z_o)$ are plotted in Fig. 40.

Since the variations in stresses associated with Rayleigh waves are considered smaller than those which are obtained around crack tips, it is speculated that distances z_o for a best visualization of Rayleigh wave shadow patterns must be larger than those for crack tip shadow patterns. Consequently, if the distance z_o is reduced to a value smaller than the optimum distance, then the reduction in the shadow optical effect is expected to be larger for Rayleigh wave patterns than for crack tip patterns.

In order to prove this hypothesis shadow optical pictures for Raleigh wave disturbances had been photographed with different distances z_o of 0.75 m, 0.4 m, 0.2 m (Fig. 41). As expected, the disturbances are less pronounced with smaller distances z_o. Fig. 42 shows shadow optical patterns of both the Raleigh wave disturbances and the crack tip patterns for two distances z_o, 1.5 m and 0.75 m. The distance z_o = 1.5 m is the optimum distance for a best visualization of crack tip patterns which was used in the previous contract for measuring fracture toughness values at high loading rates. A reduction in the shadow optical sensitivity, has a larger effect on the Rayleigh wave disturbances than on the crack tip patterns, as was expected. The crack tip shadow pattern observed at a distance z_o = 0.75 m is smaller than that for z_o = 1.5 m but is still sufficiently large for reliable quantitative evaluations. Rayleigh wave shadow patterns, however, are very much reduced in their intensity and the disturbances now allow a better and less disturbed measurement of the size of the crack tip shadow patterns. With this improved shadow optical arrangement most of the experiments of this report have been performed.

This procedure, the reduction of the observation distance, however, has consequences which have to be taken into consideration. With a real material limitations arise by the size of the plastic zone represented by its radius r_{pl}. This quantity is given according to ASTM E 616 for plain stress

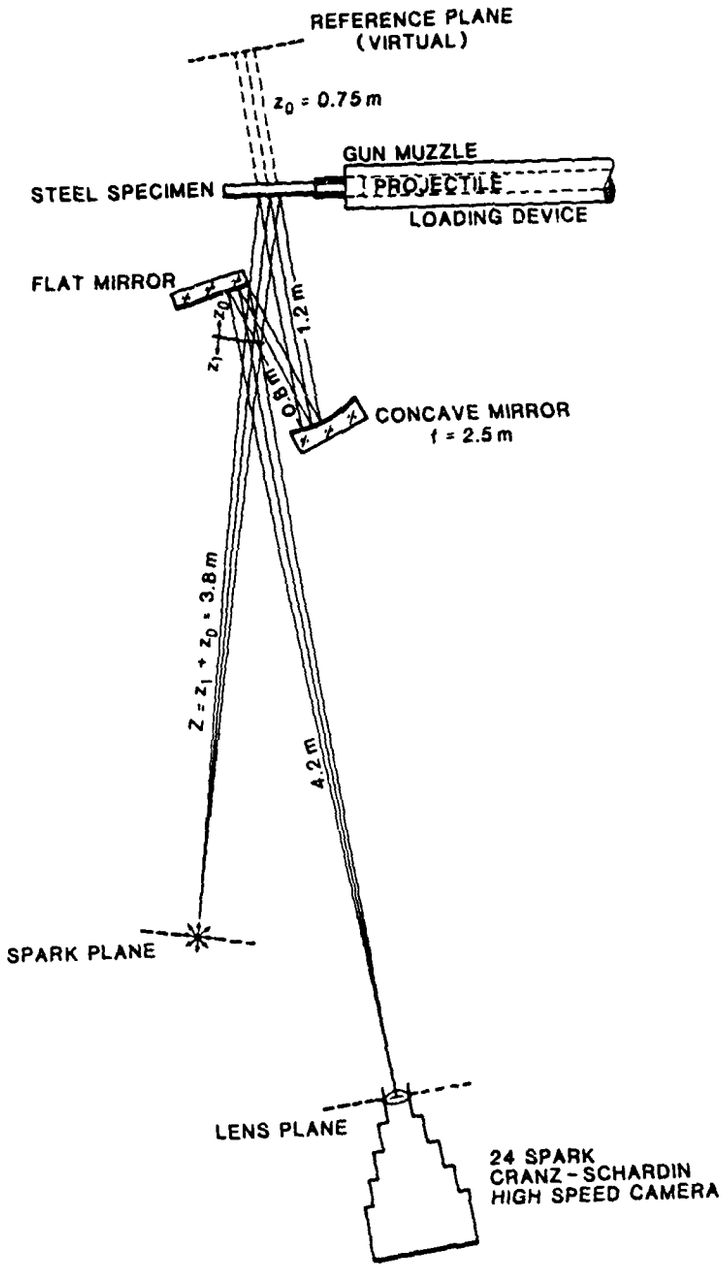

Fig. 39 Shadow optical recording arrangement for convergent light in reflection; optimized with very narrow light tracing (reflection angles 17°)

conditions by

$$r_{pl} = \frac{1}{2\pi}\left[\frac{K}{\sigma_Y}\right]^2 \qquad (4)$$

This is illustrated with the yield strength as a parameter by Fig. 43. A reduced distance z_o of the shadow optical image plane reduces also the radius r_o of the initial curve on the specimen surface which depends on this distance as well as on the applied stress intensification K:

$$r_o = \left[\frac{3Kz_oc(d/2)}{2\sqrt{2\pi}m}\right]^{2.5} \qquad (5)$$

This formula is illustrated for the conditions z_o = 0.75m, Z = 3.8m and a specimen thickness of 20mm and the material parameters ν = 0.32 and E = 183 GPa by Fig. 41. The decrease of this circle with the decreasing distance of the reference plane causes new errors when the radius of the plastic zone becomes comparable with the radius of the initial curve because of the no longer fulfilled condition of small scale yielding on which the theory of the shadow optical method is based.

Fig. 44 is an example for a very specific material (the high strength steel X2 NiCoMo 18 9 5, with the parameters σ_Y = 2 GPa, K_{Ic} = 70 MPa$\sqrt{m}$, which results in r_{pl} = 1 mm, Young's modulus E = 183 GPa and Poisson's ratio ν = 0.32) and for the specific experimental conditions of Fig. 39). Changing the material or the optical arrangement demands the calculation of a new set of curves. These figures, however, demonstrate that for most materials and for suitable optical conditions both radii are of comparable size. If this is true (which is fortunately not the case with the high strength steel) there is presently only one way to get reliable results: a calibration curve where the shadow spot diameter is related to the mechanically determined stress intensity factor has to be established in static experiments.

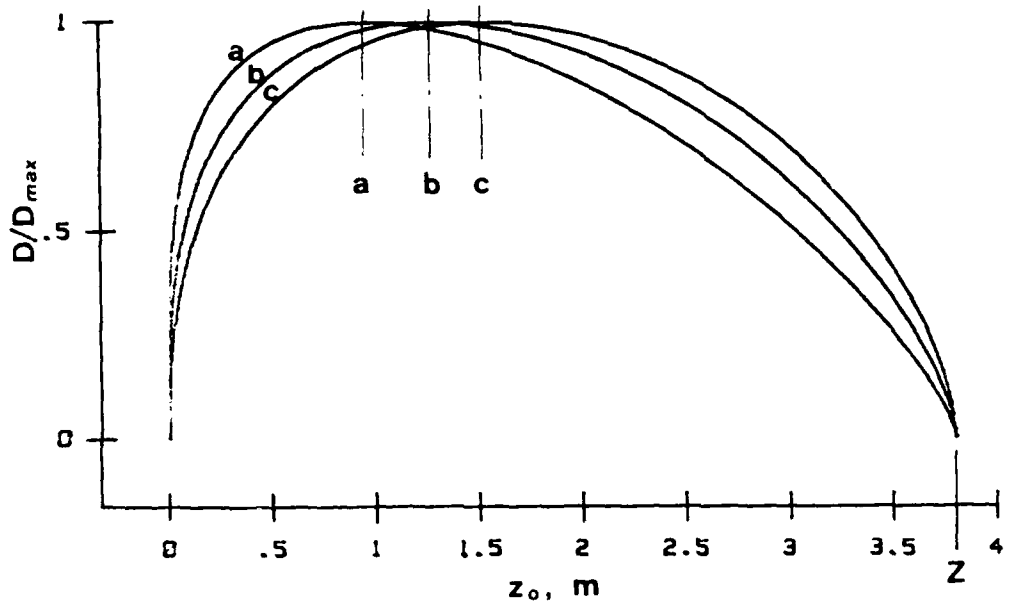

Fig. 40 Dependence of the size D of a shadow pattern on the distance z_o between specimen surface and reference plane for a given distance Z (light source to specimen suface) of 3.8 m and for the three problems a, b, and c of Fig. 38

Fig. 41 Shadow patterns of Rayleigh wave disturbances photographed at different distances z from the specimen

Fig. 42 Shadow patterns of crack tips and Rayleigh wave disturbances photographed at differrent distances z from the specimen

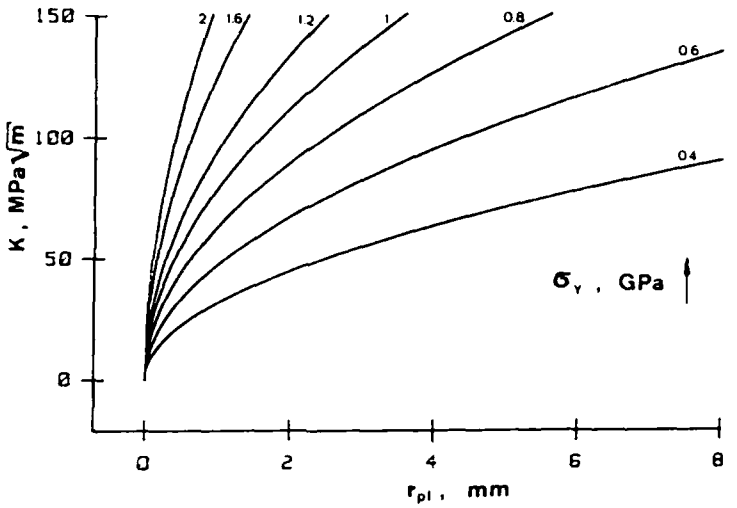

Fig. 43 Relationship between plastic zone size, yield strength and stress intensity factor K

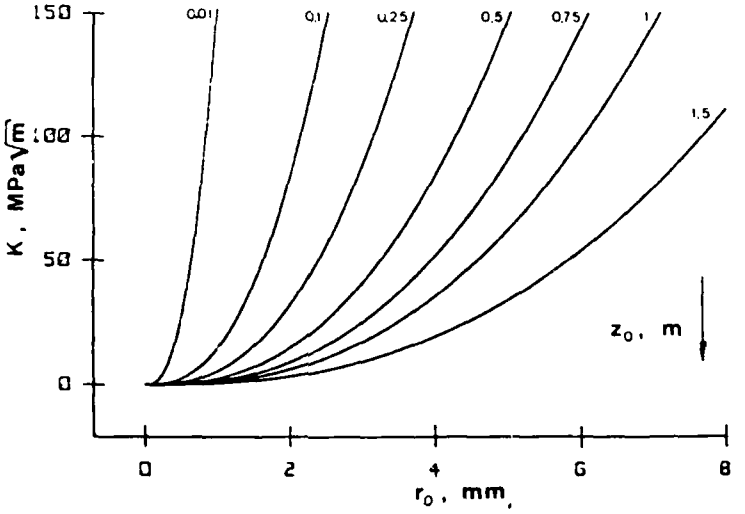

Fig. 44 Relationship between radius r_o of the initial curve, distance z_o of reference plane from specimen, and stress intensity factor K for the specific optical arrangement of Fig. 39

6. APPENDIX
THE SHADOW OPTICAL METHOD OF CAUSTICS

The method of caustics is an optical tool for measuring stress concentrations. It was introduced by Manogg [6] in 1964 and has been developed further later on by Theocaris et al. [7, 8], Rosakis [9], and Kalthoff et al. [10, 11].

The physical principal of the shadow optical method of caustics is illustrated in Fig. A1. A cracked specimen subjected to mode I tensile loading is illuminated from the left side by a parallel light beam. The specimen is made from a transparent material. A cross section through the specimen near the crack tip is shown on the right side of the figure. Due to the stress concentration at the crack tip the physical conditions are changed: The thickness of the specimen and the refractive index of the material are reduced. Consequently, the area surrounding the crack tip behaves in a manner similar as a divergent lens deflecting light rays outwards. However, in this case light deflection is the larger the nearer to the crack tip the light beam traverses the specimen. Consequently, on a screen at a distance z_0 behind the specimen a shadow pattern is observed which is surrounded by a bright light concentration area, the focal line or caustic. The size of the shadow pattern is a quantitative measure of the stress intensity factor K at the crack tip.

Shadow patterns cannot only be observed in real image planes which is in observation direction before the specimen, as is illustrated in Fig. A1. Also virtual shadow patterns in virtual image planes (behind the specimen) can be made visible and recorded if a lens is used for transformation into the real space. This can be done by the lens of a camera. In analogy to the considered transmission arrangement shadow patterns can also be observed with non-transparent materials in reflection (the specimen surface has to be a mirror). In these cases the light beam deflection is caused by deformations on the specimen surface only. In reflection the observation direction is reverse with regard to the transmission arrangement, but similar to the transmission case real or virtual shadow patterns can be observed in observation direction before respectively behind the specimen. Furthermore, analogous to the tensile mode I loading case considered in Fig. A1 shadow patterns can also be observed for compressive mode I loading conditions and under shear mode II loading conditions.

Calculated caustics and light intensity distributions of various shadow patterns are shown in Fig. A2. These can be observed in real and virtual image planes with cracks under positive and negative mode I or mode II loading conditions

in transmission or in reflection recording arrangements. In principal, any kind of caustic observed under any observation mode can be used for quantitative determination of stress intensity factors. For the mode I loading case, however, it is appropriate choosing a recording arrangement that leads to a caustic of the form (a) since shadow spots can be evaluated more accurately than the light concentration configuration (b). With the characteristic length parameters D defined in Fig. A2 the stress intensity factors K_I and K_{II} are determined by the relations

$$K_I = \frac{1}{m^{3/2}} \frac{2\sqrt{2\pi}}{3(3.17)^{5/2} z_o c d_{eff}} D^{5/2} \qquad (A1)$$

$$K_{II} = \frac{1}{m^{3/2}} \frac{2\sqrt{2\pi}}{3(3.02)^{5/2} z_o c d_{eff}} D^{5/2} \qquad (A2)$$

with

K_I, K_{II} = stress intensity factors for mode I, mode II loading condition, respectively

D = diameter of the caustic (see Fig. A1)

z_o = distance between the shadow optical image plane and the specimen ($z_o \neq 0$ for real image planes, $z_o > 0$ for virtual image planes)

c = shadow optical constant
= $-0.97 \cdot 10^{10}$ 1/Pa for Araldite B in transmission
= $-1.08 \cdot 10^{10}$ 1/Pa for PMMA in transmission
= $2\nu/E$ for all materials in reflection

d_{eff} = effective specimen thickness
= d for transparent specimens in transmission
= d/2 for opaque specimens in reflection

d = physical thickness of the specimen.

m = $(Z - z_o)/Z$, scaling factor; m = 1 for parallel light (see Fig. 42)

For superimposed mode I - mode II loading conditions mixed mode caustics are obtained which allow a determination of both stress intensity factors, K_I and K_{II} .

For the practical application of the caustic technique the caustic curves and the light intensity distributions shown

in Fig. A2 as well as the the eqs. (A1) and (A2) have to be modified: With optically anisotropic materials like Araldite B, for example, the single caustic curve considered so far splits up into a double caustic, and with non-parallel light beams which are used in most practical applications additional scaling factors, m, are necessary in eqs. (A1) and (A2). A review on the shadow optical method of caustics and its applications is given in [4].

Shadow optical pictures for transient problems are recorded with a Cranz-Schardin 24 spark high speed camera with a minimum picture interval time of 1 µs. The camera is triggered by a laser beam which is interrupted by the projectile before it hits the specimen.

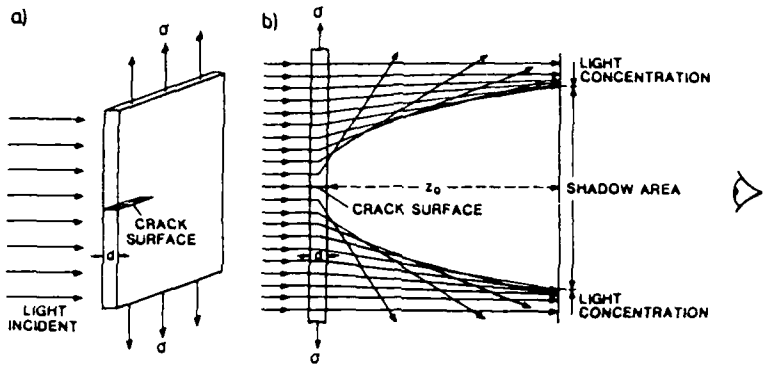

Fig. A1 Principle of the shadow optical method of caustics

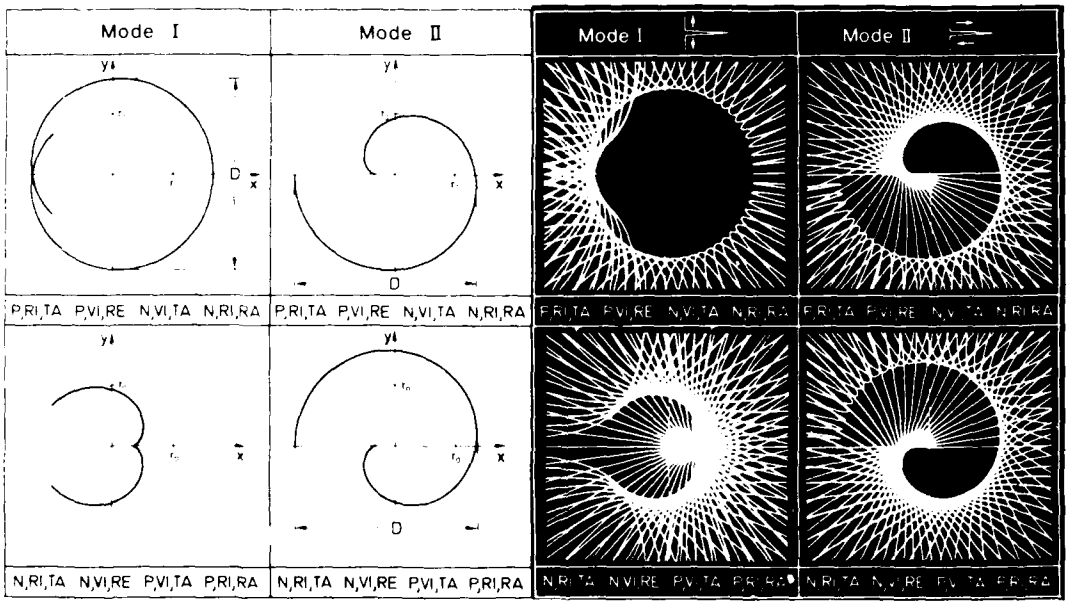

Fig. A2 Calculated caustics (left) and calculated light distributions (right). Symbols: P,N = pos., neg. loading; RI, VI = real, virtual image plane; TA, RA = transmission, resp. reflection arrangement

7. REFERENCES

[1] Kalthoff, J.F. and S. Winkler: "Fracture Behavior Under Impact", Final Report W 10/86, prepared for US ERO, Fraunhofer-Institut fur Werkstoffmechanik, 1986

[2] Ravi-Chandar, K. and W.G. Knauss: "An Experimental Investigation into Dynamic Fracture: I. Crack Initiation and Arrest", Int.J.Fract. 25, pp. 247-262, 1984

[3] Creager, M. and P.C. Paris: "Elastic Fields Equations for Blunt Cracks with Reference to Stress Corrosion Cracking", Int.J.Fract.Mech. Vol.3, pp. 247-252, 1967

[4] Kalthoff, J.F.: "The Shadow Optical Method of Caustics", Handbook on Experimental Mechanics, Ed. A.S. Kobayashi, Prentice Hall, N.J., pp. 430-500, 1986

[5] Kalthoff, J.F.: "The Concept of Impact Response Curves", in Metals Handbook, Vol. 8, Mechanical Testing, American Society for Metals, Metals Park, Ohio, 1985

[6] Manogg, P.: " Anwendung der Schattenoptik zur Untersuchung des Zerreißvorgangs von Platten", Dissertation, Universität Freiburg, 1964

[7] Theocaris, P.S. and N. Joakimides: "Some Properties of Generalized Epicycloids Applied to Fracture Mechanics", J. Appl. Mech., 22, pp. 876-890, 1971

[8] Theocaris, P.S.: "Complex Stress Intensity Factors of Bifurcated Cracks", J. Mech. Phys. Solids, 20, pp. 265-279, 1972

[9] Rosakis, A.J. and L.B. Freund: "Optical Measurement of the Plastic Strain Concentration at a Tip in a Ductile Steel Plate", J. Eng. Mat. Technol., 104, pp. 115-125, 1982

[10] Kalthoff, J.F., S. Winkler, and J. Beinert: "Measurements of Dynamic Stress Intensity Factors for Fast Running and Arresting Cracks in Double-Cantilever-Beam Specimens", Fast Fracture and Crack Arrest, ASTM STP 627, Eds. G.T. Hahn and M.F. Kanninen, American Society for Testing and Materials, Philadelphia, pp. 161-176, 1977

[11] Kalthoff, J.F., W. Bohme, and S. Winkler: "Analysis of Impact Fracture Phenomena by Means of the Shadow Optical Method of Caustics", Proc. 7th Int. Conf. Exp. Stress Anal., pp. 148-160, organized by SESA, Haifa, Israel, Aug. 23-27, 1982

[12] Kalthoff, J.F. and S. Winkler: "Fracture Behavior under Impact", Third Periodic Report (First Annual Report) V 37/86, prepared for US ERO, Fraunhofer-Institut für Werkstoffmechanik, 1986

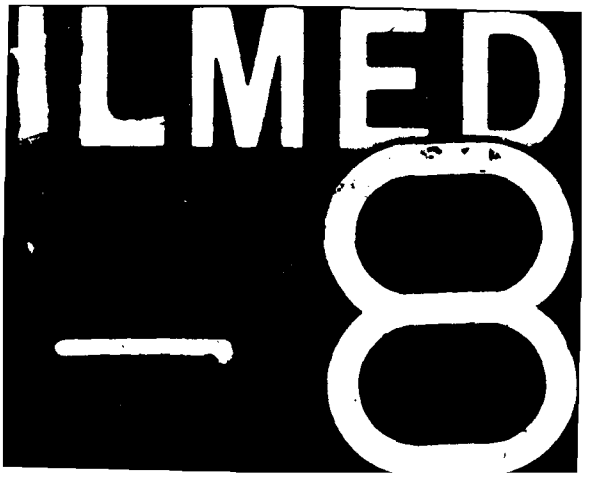
ILMED
8